DTU Library

Multiphysics modelling of manufacturing processes: A review

Jabbari, Masoud; Baran, Ismet; Mohanty, Sankhya; Comminal, Raphaël; Sonne, Mads Rostgaard; Nielsen, Michael Wenani; Spangenberg, Jon; Hattel, Jesper Henri

Special Issue Article

Multiphysics modelling of manufacturing processes: A review

Masoud Jabbari[1], Ismet Baran[2], Sankhya Mohanty[3], Raphaël Comminal[3], Mads Rostgaard Sonne[3], Michael Wenani Nielsen[4], Jon Spangenberg[3] and Jesper Henri Hattel[3]

Abstract
Numerical modelling is increasingly supporting the analysis and optimization of manufacturing processes in the production industry. Even if being mostly applied to multistep processes, single process steps may be so complex by nature that the needed models to describe them must include multiphysics. On the other hand, processes which inherently may seem multiphysical by nature might sometimes be modelled by considerably simpler models if the problem at hand can be somehow adequately simplified. In the present article, examples of this will be presented. The cases are chosen with the aim of showing the diversity in the field of modelling of manufacturing processes as regards process, materials, generic disciplines as well as length scales: (1) modelling of tape casting for thin ceramic layers, (2) modelling the flow of polymers in extrusion, (3) modelling the deformation process of flexible stamps for nanoimprint lithography, (4) modelling manufacturing of composite parts and (5) modelling the selective laser melting process. For all five examples, the emphasis is on modelling results as well as describing the models in brief mathematical details. Alongside with relevant references to the original work, proper comparison with experiments is given in some examples for model validation.

Keywords
Numerical modelling, tape casting, nanoimprint lithography, extrusion, composite, selective laser melting

Introduction

Numerical modelling is increasingly being used in the design and optimization of manufacturing processes in order to increase the quality of the produced parts and improved production yield. Today, complex manufacturing processes are often addressed with multiphysics models involving numerical heat transfer, computational fluid dynamics (CFD) and computational solid mechanics (CSM) as well as thermodynamic and kinetic models.[1] Progress in numerical modelling of material behaviour, efficient computational algorithms and advances in computer hardware and storage devices have increased the ability of complex software to be used for process design and optimization.[2]

Mathematical flow simulations, also known as CFD, have matured rapidly in the last half-century.

Particularly, in the manufacturing industry, use of CFD normally leads to reduced design time/cycle and improved process performance. CFD has been extensively used in metal casting and simulating the flow of molten metals in moulds.[3–6] Reilly et al.[7,8] have critically reviewed the role of CFD in defect entrainment in

[1]WMG, The University of Warwick, Coventry, UK
[2]Faculty of Engineering Technology, University of Twente, Enschede, The Netherlands
[3]Department of Mechanical Engineering, Technical University of Denmark, Kongens Lyngby, Denmark
[4]LM Wind Power A/S, Lunderskov, Denmark

Corresponding author:
Masoud Jabbari, WMG, The University of Warwick, Coventry CV4 7AL, West Midlands, UK.
Email: M.Jabbaribehnam@Warwick.ac.uk

the shape casting process and summarized different numerical approaches used in different commercial packages, that is, MAGMASOFT[9] and FLOW-3D.[10] Another example of fluid flow analysis in modelling of manufacturing processes has been given by Zhang and Wu,[11] in which they investigated the effect of fluid flow in the weld pool on the numerical simulation accuracy of the thermal field in hybrid welding.

The use of CSM as another field of interest in numerical modelling of manufacturing process has also dramatically increased during the last decades. In most cases, CSM analysis is coupled with numerical heat transfer models. As an example, Schmidt et al.[12,13] developed an analytical/numerical model for simulating heat generation in friction stir welding (FSW), which is based on different assumptions of the contact condition between the weld piece and the rotating tool surface. Schmidt and Hattel[14] have developed a fully coupled thermomechanical three-dimensional model for FSW using the arbitrary Lagrangian–Eulerian formulation combined with the Johnson–Cook (J-C) material law. In another study, Sonne et al.[15] studied the effect of hardening laws and thermal softening on modelling residual stresses in FSW of aluminium alloys. In their work, the Thermal Pseudo Mechanical (TPM) model is sequentially coupled with a quasi-static stress analysis incorporating a metallurgical softening model. Multiphysics modelling of welding has recently been combined with optimization methods to obtain desired properties of the weld.[16] Numerical analysis of FSW has been reviewed in the literature in general[17] and with an especial focus on modelling residual stresses.[18]

The basis of most numerical simulation of high temperature processes is a proper thermal model which in many cases would be coupled with models describing kinetic and/or thermodynamic phenomena. This is very much the case for the metal casting industry which still today is a main provider of a large amount of all manufactured parts. In contrast to the traditional experimental based design of casting,[19,20] numerical simulation holds great potential for increasing the productivity in the foundry industry by shortening production time. This field has been active for many years and there is still increasing effort in further developing the numerical simulation tools for variety of different casting processes.[21,22]

In the following, five different examples of manufacturing processes and their numerical analysis will be presented. A short introduction to each process will be given followed by some important results. The models for each of the examples will only be explained in brief; however, proper references to the original work will be given, in case more specification is needed. The selected examples are as follows:

1. Modelling of tape casting for thin ceramic layers;
2. Modelling the flow of polymers in extrusion;
3. Modelling the deformation process of flexible stamps for nanoimprint lithography (NIL);
4. Modelling manufacturing of composite parts;
5. Modelling the selective laser melting (SLM) process.

The two first examples deal with modelling of fluid flow, while the following two examples treat thermomechanical modelling, and finally, the last example employs a thermo-metallurgical model.

Modelling of tape casting

Tape casting is one of ceramic processes used to produce multilayer parts and substrates, like for example, capacitors, piezoelectric actuators, gas sensors.[23,24] In this process, the ceramic slurry contains different ingredients, which in general influence on the rheological behaviour of the ceramic flow by increasing the viscosity magnitude and/or its non-linear dependence on shear rate (also known as non-Newtonian behaviour).[25–32] However, this does not mean that assuming Newtonian (linear) explanation for the viscosity of ceramic is wrong.[33,34]

Fluid flow analysis in tape casting and especially in the doctor blade region and the casting reservoir (see Figure 1) is one of the most important fields of study, as it directly influences on the produced tapes. This has been the focus of researchers by developing closed-form analytical solution for the Navier–Stokes equations (combined Couette and Poiseuille flow).[27–36] However, such models are limited to predicting flow front (meniscus), and hence, tape uniformity as well as thickness variation. Numerical modelling of tape casting instead will
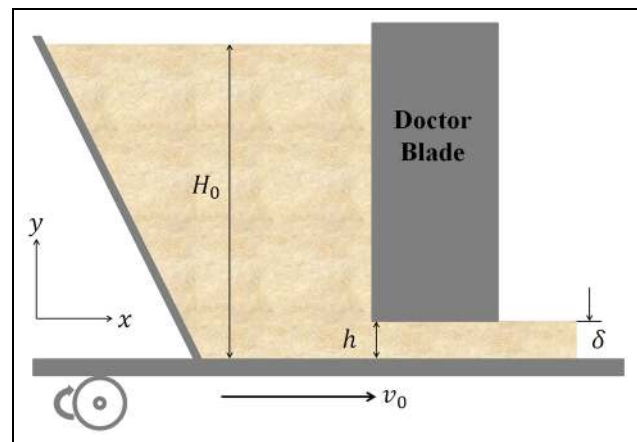

Figure 1. 2D schematic of the tape casting process.[35]

lead to optimizing the process by simulating more advanced features related to flow analysis.[26,37–42]

For fluid flow analysis in tape casting normally the coupled momentum and continuity equations should be solved, that is

$$\rho \left(\frac{\partial \boldsymbol{u}}{\partial t} + \boldsymbol{u} \cdot \nabla \boldsymbol{u} \right) = -\nabla p + \nabla \cdot \mathbf{T} + \mathbf{F} \qquad (1)$$

$$\frac{\partial \rho}{\partial t} + \nabla \cdot (\rho \boldsymbol{u}) = 0 \qquad (2)$$

where ρ is density (kg/m^3), t is time (s), $\boldsymbol{u}$ is velocity vector, p is pressure (Pa), $\mathbf{T}$ is viscous stress tensor (Pa) and $\mathbf{F}$ is the contribution from external forces. These equations can be solved either analytically (one would have to do quite some modifications/simplifications of the equations to solve them analytically) or numerically, in combination with a proper constitutive law (here the rheological behaviour). In Cartesian co-ordinates, the governing equation of the shear stress (for an incompressible fluid) can be given as

$$\underline{\underline{\tau}} = \mu \underline{\dot{\gamma}} \qquad (3)$$

where μ is the dynamic viscosity, $\underline{\underline{\tau}}$ is the shear stress tensor (Pa) and $\underline{\dot{\gamma}}$ is the shear rate tensor (Pa s). Here $\underline{\dot{\gamma}}$ is the rate of the strain tensor, $\underline{\dot{\gamma}} = \nabla \boldsymbol{u} + \nabla \boldsymbol{u}^{\top}$, which is given by

$$|\dot{\gamma}| = \sqrt{\frac{1}{2} II_{\dot{\gamma}}} = \left[\frac{1}{2} \left\{ \underline{\dot{\gamma}} : \underline{\dot{\gamma}} \right\} \right]^{1/2} \qquad (4)$$

in which $II_{\dot{\gamma}}$ is the second invariant of $\dot{\gamma}$, $\nabla \boldsymbol{u}$ is the velocity gradient tensor and $\nabla \mathbf{u}^{\top}$ is its transpose. For the stress tensor, $\underline{\underline{\tau}}$, similarly we have

$$|\tau| = \sqrt{\frac{1}{2} II_{\tau}} = \left[\frac{1}{2} \left\{ \underline{\underline{\tau}} : \underline{\underline{\tau}} \right\} \right]^{1/2} \qquad (5)$$

where II_{τ} is the second invariant of $\underline{\underline{\tau}}$. In general, it is the correlation between shear stress and shear rate that defines the (rheological) nature of a fluid. Fluids with linear correlation fall into Newtonian category and they have constant dynamic viscosity, μ, as a slope in their flow diagram, for example, equation (3). As mentioned earlier, assuming Newtonian behaviour will reduce simulation complexities/efforts yet producing fair results.[33,34,38] However, it is more realistic to describe the ceramic slurry as a non-Newtonian fluid, where τ is a non-linear function of $\dot{\gamma}$. The most commonly used/reported constitutive models of non-Newtonian behaviour are the shear thinning power-law and the Bingham material models,[25–27,29–32,35,36,40–43] and they are given as follows

$$\underline{\underline{\tau}} = \mu_a \underline{\dot{\gamma}}^n, \quad \mu_a = k \underline{\dot{\gamma}}^{n-1} \qquad (6)$$

$$\begin{aligned} \underline{\underline{\tau}} &= \left(\mu_B + \frac{\tau_y}{|\dot{\gamma}|} \right) \underline{\dot{\gamma}} & |\tau| > \tau_y \\ \underline{\dot{\gamma}} & & |\tau| \le \tau_y \end{aligned} \qquad (7)$$

where μ_a is the apparent viscosity (Pa s), n is the power-law index and k is the consistency for a power-law fluid (Pa s^n), μ_B is the constant Bingham viscosity (Pa s) and τ_y is the Bingham yield point (Pa). Bingham fluids do not flow until the applied shear stress surpasses τ_y. Numerically, the yield stress is treated by introducing a very high viscosity that is active below a threshold shear rate.[44] When the stress exceeds the yield stress, τ_y, the fluid flows according to the plastic viscosity. In the following, two different numerical examples dealing with fluid flow analysis will be presented, that is, single-layered tapes and side-by-side layers, for modelling of the tape casting process. Moreover, a model for the evaporation of water from a thin layer will be presented, which takes place in the subsequent drying process.

As mentioned earlier, capturing the free surface is one of the important features in the tape casting process. An example of such investigation was first reported by Loest et al.[26,37] Jabbari et al.[41] developed a FVM-CFD model capable of tracking the free surface (using VOF method) combined with Ostwald de Waele–power-law flow behaviour. These developments have inherently allowed to study the tape casting process more in depth by attempting to simulate the important intrinsic phenomenon called the 'side flow'.[40] Side flow by definition shows amount of fluid which flows in lateral direction as it leaves the doctor blade region. Jabbari and Hattel[40] reported first of a kind in literature where the side flow factor (α) is predicted numerically. Impact of process parameters like substrate velocity (v_0) and slurry height (H_0) on α were, moreover, investigated in the same work (see Figure 2).

Dinesen et al.[45] have recently reported an application of tape casting for producing functionally graded ceramics (FGCs) by co-casting of two (or more) ceramic slurries. With main application in magnetic refrigeration parts, it is important to control the interface between different layers (see Figure 3(a)) to avoid mixing, and as a result increase the efficiency in a graded magnetocaloric material.[46] This interface in its ideal form has to be a 2D in-plane surface ($y - z$) which is perpendicular to the substrate peeling belt ($x - y$). Depending on the density or viscosity of the ceramic slurry as well as process parameters, the aforementioned interface can deviate from its ideal shape. This has been studied numerically by Jabbari et al.[47] using the FVM-CFD model developed previously,[41] by further developing for co-casting of tapes (see Figure 3(b)).
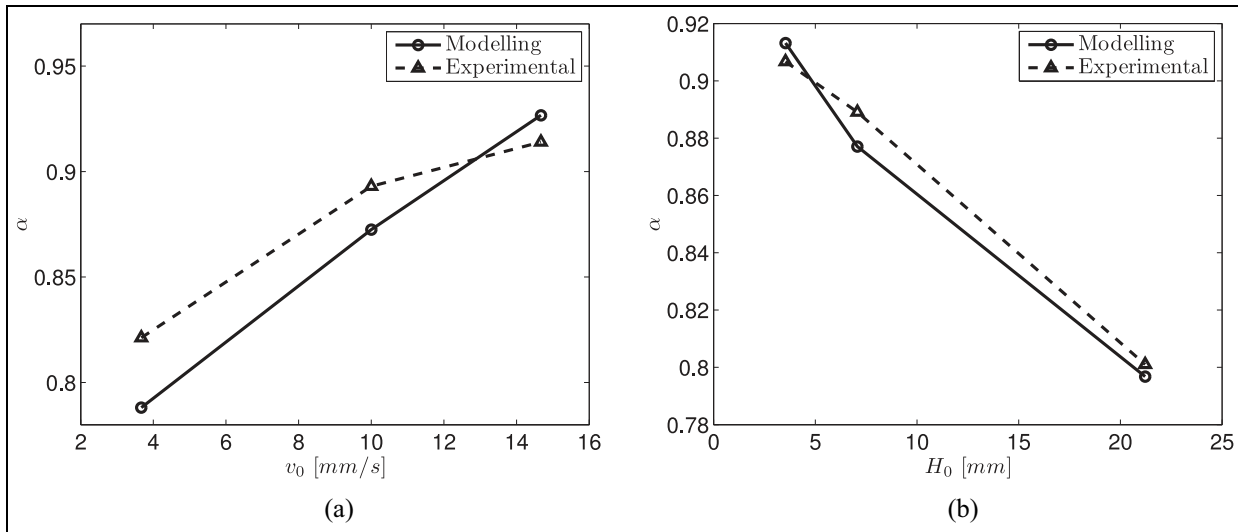
Figure 2. Modelling and experimental validation of side flow factor (α), impact of (a) peeling velocity and (b) slurry height.[40]
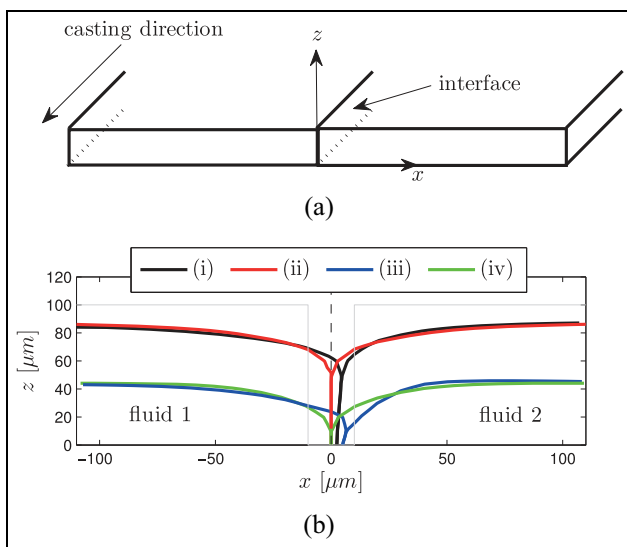
Figure 3. (a) Schematic illustration of the interface between the co-cast layers, (b) the influence of changing density and viscosity of slurry on the interface: (1) $\rho_2 = 2\rho_1$ and $\mu_2 = 2\mu_1$, (2) $\rho_2 = 2\rho_1$ and $\mu_2 = \mu_1$, (3) case 1 with doubled velocity and (4) case 2 with doubled velocity.

Such phenomenon has been verified experimentally by Bulatova et al.[48]

The second stage after producing tapes is the drying process (see Figure 4(a)), in which the solvent (water or any other liquid carrier) is removed using heat and/or ventilation.[49] In this stage, there two main mechanisms which control the rate of drying namely: (1) evaporation rate of the solvent from the top surface of the tape (in contact with air) and (2) hydraulic conductivity or the rate of solvent transport to the top surface. Different kinetics are often covered in drying, that is, mass diffusion, transport in porous media, evaporation/condensation and viscous deformation, which influence the overall drying behaviour of the ceramic tapes.

Neglecting capillary pressure (and resultant mass transport in porous media), Jabbari and Hattel[50] numerically investigated drying of tapes by developing semi-coupled heat and mass transfer (diffusion), see Figure 4(b). Assuming water to be the solvent, a mixture of ceramic and water was considered as a representation of a tape layer. This could then serve as a relevant model system for analysing the drying process in tape casting. The results of modelling are shown in Figure 5(a) for drying tapes with initial water content of 12% and different thicknesses ($\delta = 400$, 300, 200 μm). For the three tapes, there is initial period with no change on the water content. This is the time period that the tape temperature is rising without having evaporation, and as expected, this time period it the highest for the thickest tape.

Three different drying modes, that is, fast, intermediate and slow, were also investigated in Jabbari et al.[50] when $\delta = 400 \mu$m, as shown in Figure 5(b). The results showed that fast drying will result in forming an unsaturated region (solid-like) in upper half of the tape, which later on acts as a barrier for water transport (by diffusion). This will eventually reduce the drying rate for the remaining water in the tape. This may happen during drying of tapes by high heat input rates. On the other hand, in the slow drying mode, the water evaporation is somehow slow, although hydraulic conductivity supplies water for the top interface. This headlights the influence of the drying mode, and the
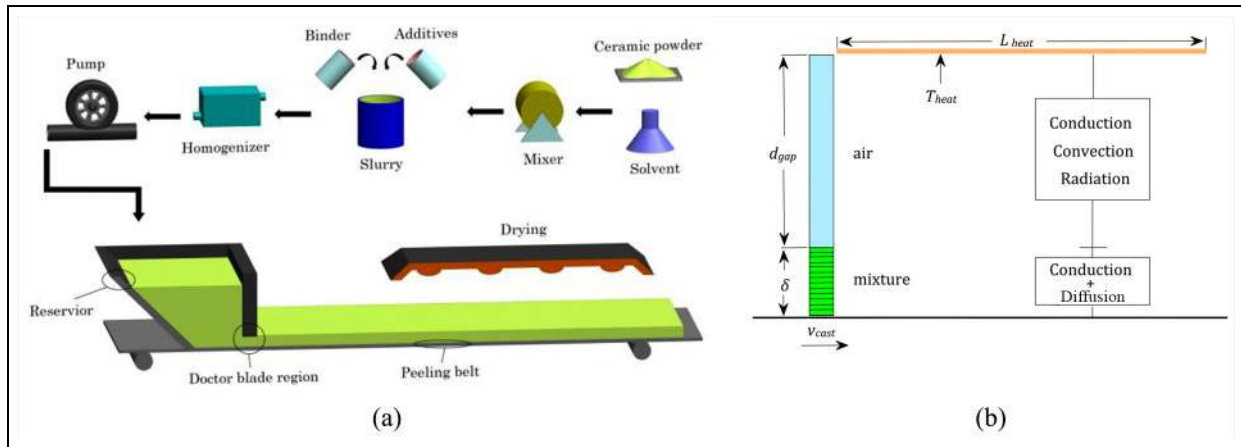
Figure 4. (a) Overall schematic of the tape casting process and the drying sub-process and (b) schematic illustration of the simulation domain.[50]
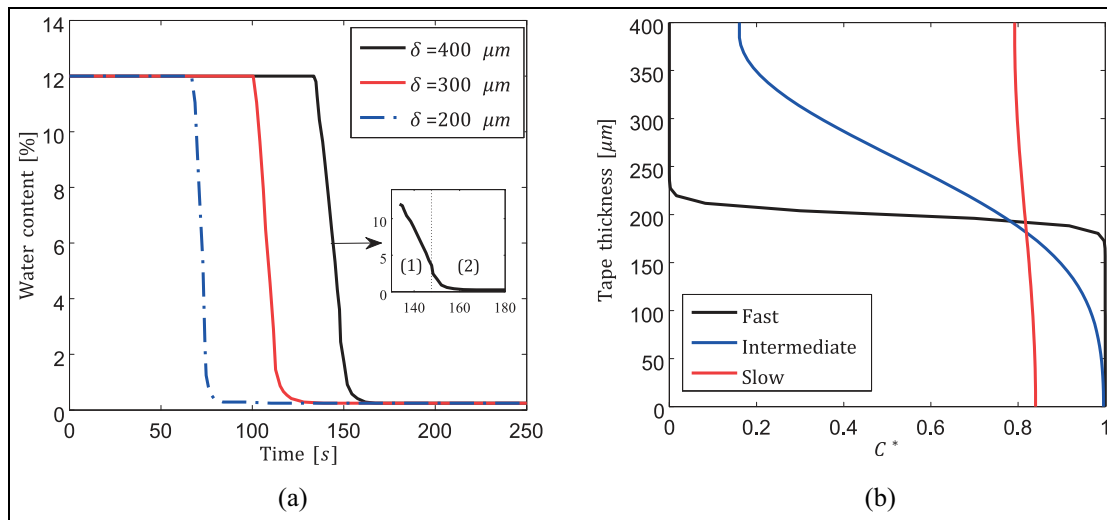
Figure 5. (a) Evaporation of water from a tape with different tape thicknesses (400, 300, 200 μm) and (b) the different drying modes for the tape thickness of $\delta = 400$ μm.[50]

competition between the already mentioned drying mechanisms (the top surface evaporation and the water diffusion from bottom to the top surface). More investigations on the drying process with high fidelity simulations using coupled free-flow–porous-media models can be found in previous works.[51–56]

Modelling the flow of polymers in extrusion

Extrusion is a common process in the plastic industry to produce long parts with a constant cross-sectional profile. The plastic material is melted and formed through a die with the desired cross-section. However, the extruded material swells at the die exit, because of

the rearrangement of the flow profile after the die exit. The flow undergoes a transition from the typical parabolic profiles inside the die (constrained by the walls), towards a uniform profile outside the die (with free surfaces at equilibrium). This phenomenon is referred to as the *extrudate swelling*. For non-axisymmetric profiles, the swelling may also produce distortions of the extrudates. Moreover, the productivity of the polymer extrusion process is often limited by flow instabilities occurring at high extrusion speeds.

The rheological properties of the extruded materials are crucial parameters for their processability (i.e. stability and flowability). The material inside the die is subjected to large shear rate deformations, which trigger the viscoelastic behaviours of the polymers due to the stretching, reorientation and disentanglement of
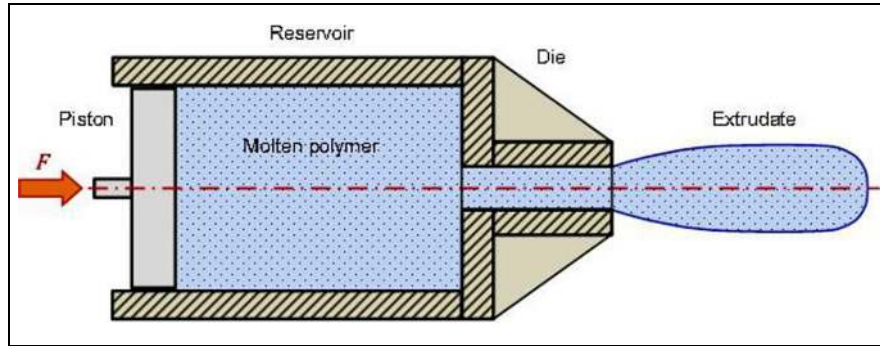
Figure 6. Schematic view of extrusion through a capillary die.

polymer chains. In contrast to generalized Newtonian fluids, elastic liquids build-up normal stress gradients when they are deformed in shear flows. Outside the die exit, the stretched polymer chains can recover their initial configuration, and the force balancing of the normal stress difference is responsible for an additional extrudate swelling (as compared to purely viscous fluids). Thus, taking the elastic effects into account – although not conventional yet – is desirable, in order to build accurate models of the polymer extrusion. Finally, the combination of non-Newtonian flow solvers developed within computational rheology with optimization algorithms will contribute to the development of powerful computer-aided manufacturing software, improving the extrusion processes via assisted or automated die design, according to specified optimization strategies (i.e. objective functions).[57–63]

The extrusion through a capillary die, sketched in Figure 6, is particularly interesting in spite of its simple geometry, because it gives an insight into the complex flow phenomena of the polymeric materials. There are different flow regimes in polymer extrusion.[64,65] Figure 7 represents the typical flow curve and the regions of instabilities for the extrusion of linear polyethylene. The vertical and horizontal axes show the wall shear stress (proportional to the pressure inside the die) and the characteristic shear rate (proportional to the throughput), respectively.

Stable extrudates with smooth surfaces are obtained at low extrusion speeds. At moderate shear rates, the sharkskin instability appears at the surface of the extrudate. The sharkskin defect produces irregular surfaces of the extrudate with superficial cracks. There is a consensus that the sharkskin defects occur at the die exit, where the material near the wall is pulled out by large tensile stress.[65,67–69] The two mechanisms currently admitted to explain the sharkskin phenomenon involve either local fractures of the polymer surface outside of the die, or a local transition between stretching and disentanglement of absorbed polymer chains inside the
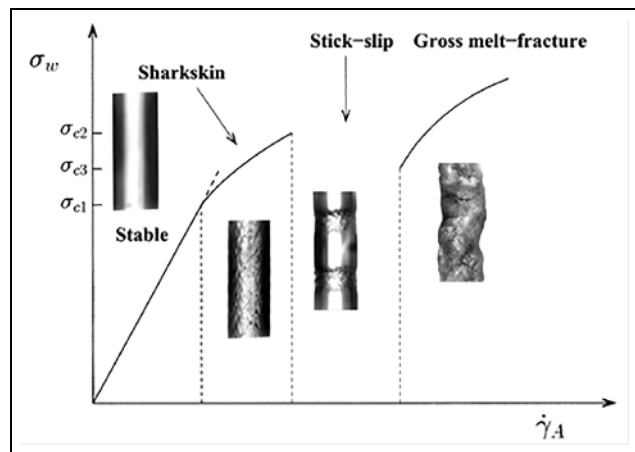
Figure 7. Typical flow curve and regions of instabilities for the extrusion a linear polyethylene (reproduced from Achilleos et al.[66] with permission).

die.[65,68,69] In both cases, stick and partial slip plays important roles in the sharkskin mechanisms.[64,65]

At larger shear rates, the extrusion experiences a stick–slip instability (or spurt phenomenon), characterized by an alternation of smooth and rough surfaces of the extrudate, and oscillations of the pressure inside the die. The numerical analyses presented in Georgiou and collegues[66,70–73] have shown that the self-sustained pressure oscillations of stick–slip instability require a non-monotonic slip law (which is consistent with both experimental data[74,75] and theoretical molecular models[76–78]), and either the compressibility or viscoelasticity of the polymer melt in the reservoir. Thus, the slip behaviour of the molten polymer on the surface of the die is a crucial phenomenon in both the sharkskin and the stick–slip instabilities. The recent review of Hatzikiriakos[79] draws a complex picture of the wall slippage of molten polymers, with two distinct slip mechanisms: flow-induced chain desorption from the wall (weak slip), and chain disentanglement of the bulk from a monolayer of absorbed chains (strong slip). Moreover, the slip mechanisms of molten polymers are

time dependent, because of the thermal degradation of absorbed polymer chains. Consequently, the inclusion of realistic slip laws in the macroscale models and the prediction of the onsets and shapes of the sharkskin and stick–slip instabilities with dynamical flow simulations are still challenging tasks. Nevertheless, the sharkskin and stick–slip instabilities can be eliminated or minimized by enhancing the slippage of the polymer, by means of chemical additives (processing aids) in the polymer formulation and/or coating on the surfaces of the die,[65,80] which results in a decrease of the wall shear stress.

At larger throughput, the flow of molten polymers is subjected to the gross melt-fracture instability, which is characterized by distortions of the extruded volume. At the onset of the gross melt-fracture, the extrudate develops regular undulated or helical shapes. The distortion of the extrudate gradually looses its periodicity and eventually evolves into a chaotic regime, when the throughput is further increased. Unlike the sharkskin and stick–slip phenomena, the gross melt-fracture originates from the bulk of the molten material and is due to the viscoelasticity of the polymers.[81,82] Observations by particle image velocimetry have shown that there are correlations between the periodic or chaotic extrudate distortions and upstream flow instabilities inside the reservoir.[83–85] The onset of gross melt-fracture can sometimes be delayed by modifications in the reservoir geometries,[65,85] without being suppressed, however. Some experimental and theoretical studies[86,87] also show that the gross melt-fracture can be due to a nonlinear subcritical instability of the viscoelastic Poiseuille flows, independent of the flow in the reservoir. Indeed, the elastic flow instabilities are intrinsic phenomena of the viscoelastic flows at low Reynolds numbers, which manifest themselves in various geometries.[88–90]

In viscoelastic flows, the relative effect of the elasticity versus the viscous forces is characterized by the *Weissenberg number*: a non-dimensional quantity relating the relaxation time λ of the material and the characteristic deformation rate of the flow. In an idealized extrusion through a capillary die, the Weissenberg number is defined as

$$Wi = \lambda U/R \tag{8}$$

where U is the average velocity in the capillary die and R is the radius of the die. Thus, the elastic effects are magnified when the extrusion speed is increased, or when the geometry of the die is downscaled.

The constitutive behaviour of viscoelastic materials does not only depend on the instantaneous deformation rate $\dot{\gamma}$, but also the history of the deformations (memory effects); thus, time is a key parameter. The stress response $\boldsymbol{\sigma}(t)$ of molten polymers can be decomposed as

$$\boldsymbol{\sigma}(t) = \eta_s \dot{\gamma} + \boldsymbol{\tau}_p \tag{9}$$

where the first term on the right-hand side corresponds to the instantaneous (purely viscous) stress response, and $\boldsymbol{\tau}_p$ is an extra-stress tensor, which is typically governed by an integral or a partial–differential model. The extra-stress accounts for elastic effects, such as stress relaxation, elastic recoil, normal stress differences. For the sake of simplicity, we assume linear viscoelasticity and use the well-known Oldroyd-B model

$$\lambda \overset{\nabla}{\boldsymbol{\tau}}_p + \boldsymbol{\tau}_p = \eta_p \dot{\gamma} \tag{10}$$

where η_p is the polymer viscosity, and

$$\overset{\nabla}{\boldsymbol{\tau}}_p \equiv \frac{\partial \boldsymbol{\tau}_p}{\partial t} + \boldsymbol{u} \cdot \nabla \boldsymbol{\tau}_p - \left(\boldsymbol{\tau}_p \cdot \nabla \boldsymbol{u}^\top + \nabla \boldsymbol{u} \cdot \boldsymbol{\tau}_p \right) \tag{11}$$

is the upper-convected time derivative, which takes into account the advection and rotation of the material in a fixed vector base. This model gives $G = \eta_p/\lambda$ as the elastic modulus, and $\eta_0 = \eta_s + \eta_p$ as the apparent steady shear viscosity.

The viscoelastic constitutive model for the extra-stress tensor is coupled with the continuity equation and the momentum conservation. These governing equations are solved with a numerical method that discretizes the geometry, for instance with finite volumes or finite elements. The Lagrangian representation of the flow (with a mesh mapped onto the deformed geometry) has demonstrated its ability to predict the steady state of stable extrusions, see for instance.[91–95] However, the Eulerian representation (with a fixed mesh) seems to be best suited for time-dependent simulations with free surface flows.[96] Eulerian models have been used to simulate extrudate swelling in the stable flow regime, where the free surface outside the die was represented via an explicit surface-tracking technique, see for instance.[97–99] Recent results of Tomé et al.[99] show that Tanner's theory,[100,101] which provides approximate analytical solutions of the extrudate swelling from capillary dies, did not predict the correct relation of the swelling ratio with the Weissenberg number. At large extrusion rates, the numerical simulations show a linear relation, while Tanner's theory predicted a cubic-root dependency. Nonetheless, for Weissenberg numbers below unity, Tanner's theory provides acceptable results which fit experimental data well.[102]

Despite promising results, the numerical simulation of viscoelastic liquids is prone to an inherent numerical instability, referred to as the *high Weissenberg number problem*, which manifests itself by the breakdown of the simulation (i.e. blow-up of numerical values), when the Weissenberg number reaches a critical value.[103,104] This has been a long-standing challenge of computational rheology, and the origins of the problem have

been understood only recently. The simulations crash when the conformation tensor

$$c = \frac{\tau_{\mathrm{p}}}{G} + \mathbf{I} \qquad (12)$$

a non-dimensional internal variable representing the strain of the polymer chains, which should be symmetric positive definite by definition,[105] looses its positive definiteness.[105–107] Moreover, the loss of positive definiteness happens because of numerical errors dues to under-resolution of the spatial stress profiles,[108,109] which may have steep gradient variations and/or be exponential, near the boundary layers and geometrical singularities.[110] A seminal reformulation of the differential constitutive model (3) has been proposed by Fattal and Kupferman.[107,108] The problem is removed by a change of variable using the matrix-logarithm of the conformation tensor

$$\mathbf{\Psi} = \log(\boldsymbol{c}) \qquad (13)$$

In terms of $\boldsymbol{\psi}$, the exponential stress profiles become linear and are easily resolvable. An evolution equation for the log-conformation tensor is derived as

$$\frac{\partial \mathbf{\Psi}}{\partial t} + \boldsymbol{u} \cdot \nabla \mathbf{\Psi} - (\mathbf{\Omega}\mathbf{\Psi} - \mathbf{\Psi}\mathbf{\Omega}) - 2\mathbf{E} = \frac{1}{\lambda}[\exp(-\mathbf{\Psi}) - \mathbf{I}]$$
$$(14)$$

where $\mathbf{\Omega}$ and $\mathbf{E}$ are anti-symmetric (pure rotation) and symmetric traceless (pure extension) matrices that compose the velocity gradient $\nabla \boldsymbol{u}$, see Fattal and Kupferman[107] for more details. Finally, the recovery of the conformation tensor by the matrix-exponential operation $\boldsymbol{c} = \exp(\mathbf{\Psi})$ automatically enforces the positive definiteness. The log-conformation representation was a breakthrough that has opened new possibilities in the simulations of the viscoelastic flows dominated by elastic effects, like in the gross melt-fracture for instance, which were not accessible before.

To the knowledge of the authors, the recent work of Kwon[111] is the only attempt of direct numerical simulations of the gross melt-fracture instability that have been reported in the literature. Kwon simulated the flow of an elastic liquid through a two-dimensional extrusion die, using the log-conformation representation with the Leonov constitutive model.[112] The geometry of the simulation included two rectilinear sections with an abrupt contraction, representing the die and the extruder reservoir. Kwon's model neglects the inertia and the slip of the polymer melt on the die's wall (i.e. no-slip boundary condition). The free surface of the extrudate was tracked with the Level-Set method.[113] The results presented different types of unstable extrusions, where some are qualitatively similar to the gross melt-fracture defect. The simulations showed that these extrusion instabilities originate from flow instabilities emanating from various locations within the die and reservoir, and which are only attributable to elastic effects.

A similar modelling approach has been employed by Comminal,[114] to simulate two-dimensional viscoelastic flows at the exit of a slit die. Comminal et al.[115] applied the same hypothesis as Kwon of an inertialess flow and no-slip at the walls, but used the log-conformation representation with the Oldroyd-B model and a viscosity ratio $\eta_{\mathrm{p}} = 8\eta_{\mathrm{s}}$. Moreover, Comminal et al. utilized a pressureless reformulation of the conservation laws in terms of streamfunctions,[115–117] defined as the vector potential of the incompressible velocity field (Helmholtz decomposition)

$$\boldsymbol{u} = \nabla \times \mathbf{\Phi} \qquad (15)$$

In two dimensions, the in-plane velocity components are solely defined by the out-of-plane component ϕ_z of the streamfunction vector

$$u_x = \frac{\partial \phi_z}{\partial y}, \quad u_y = -\frac{\partial \phi_z}{\partial x} \qquad (16)$$

and ϕ_z is governed by the following evolution equation (derived from the curl of the momentum equations)

$$\rho \frac{\partial}{\partial t}\left(\nabla^2 \phi_z\right) = \eta_{\mathrm{s}}\nabla^4 \phi_z + \nabla \times \left(\nabla \cdot \boldsymbol{\tau}_{\mathrm{p}}\right) \qquad (17)$$

The streamfunction formulation removes the pressure unknown and automatically fulfils the mass conservation, by construction, in virtue of the following vector calculus identities

$$\nabla \cdot (\nabla \times \mathbf{\Phi}) = 0, \ \forall \mathbf{\Phi} \in \mathbb{R}^3 \qquad (18)$$

$$\nabla \times (\nabla p) = 0, \ \forall p \in \mathbb{R} \qquad (19)$$

The pressureless formulation removes potential flaws due to the coupling of the pressure with the velocity and the extra-stress. Numerical investigations in the lid-driven cavity have shown an enhancement of the accuracy and robustness of the viscoelastic simulations.[118]

In contrast to Kwon, Comminal et al.[118] modelled a slit die without reservoir (no contraction geometry). Moreover, the symmetric boundary condition was applied at the mid-plane of the die, to limit the computational costs. Hence, the simulations of unstable extrusions are constrained to solutions with a symmetric mode. The free surface of the extrudate was tracked with a recently developed volume-of-fluid advection scheme.[120] The results present stable extrudates, for low throughputs only. At the moderate Weissenberg number $Wi = 1.5$, the extrudate is unstable but has a surface with wavy undulations coming from regular fluctuations in the stress boundary layer inside the die,
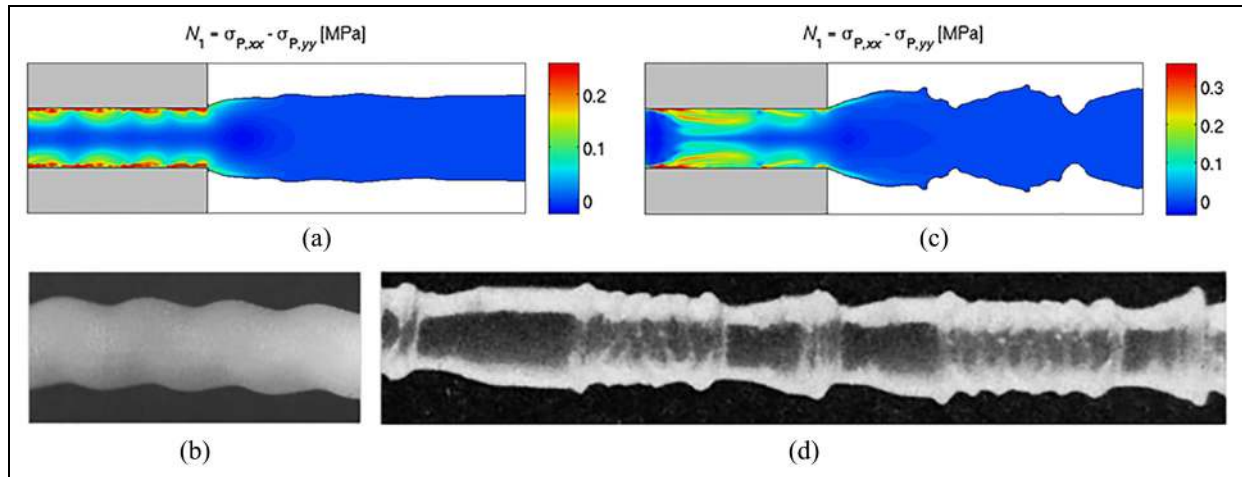
Figure 8. Simulated free surfaces of the extrudate and first normal stress differences inside the die, (a) for $Wi = 1.5$ and (c) for $Wi = 6$. (b) Wavy distortion of HDPE extrudate with an apparent shear rate of $500\,s^{-1}$; reproduced from Kalika and Denn[122] with permission. (d) Transition regime of the stick–slip instability of a LLDPE extrudate with an apparent shear rate of $985\,s^{-1}$; reproduced from Kalika and Denn[122] with permission.

see Figure 8(a) and (b). Another type of instability is visible at the larger Weissenberg number of $Wi = 6$, with a more complex shape of the extrudate, see Figure 8(c). In spite of the enforced no-slip boundary condition, elastic stress instabilities emulate cohesive failures that are qualitatively similar to those of the stick–slip phenomenon. As a result, the simulated free surface resembles that of the transition regime of the stick–slip instability observed in Figure 8(d), except that the simulation does not produce the sharkskin surface. Moreover, the present model cannot truly reproduce the helicoidal instabilities as observed in real extrusions, since these are asymmetric and three-dimensional. Nonetheless, the present simulations indicate that the unstable extrusion can be caused by purely elastic instabilities arising from the parallel flow inside the die, independent of the reservoir. Noticeable fluctuations in the normal stress difference near the wall give rise to oscillations in the velocity profile, which eventually result in distortions of the extrudate outside the die. The simulated instability seems to have a periodicity, but additional investigations are necessary to confirm this observation. Finally, since the governing equation for the extra-stress tensor is hyperbolic, its solution depends on the initial and boundary values imposed at the upstream of the flow's characteristics. Thus, potential instabilities in the elastic stress are also influenced by arbitrary choices made for the extra-stress values at the inflow boundaries.[122] Moreover, the use of pre-computed, fully developed, steady-state stress profiles at the inflow boundaries may be questionable, given the proneness of viscoelastic flow towards elastic turbulence.[90]

In conclusion, it has been shown that direct numerical simulations of the gross melt-fracture phenomenon

are achievable, provided that the high Weissenberg number problem is removed, for instance with the log-conformation representation. However, further work is necessary to refine the models. To date, the simulations do not include all the complex phenomena present in polymer extrusion that are attributable to non-linear slip laws, inertia and three-dimensional effects. Nevertheless, the numerical simulations remain powerful tools to discover the underlying mechanism of the gross melt-fracture and its possible link with elastic instabilities.

Modelling the deformation process of flexible stamps for NIL

Functional nanostructures on double curved surfaces have attracted increasing attention in industry. Examples of functional nanostructures are well known from nature, where organisms and plants possess optical, adhesive and self-cleaning capabilities.[123] The scientific literature is rich in examples of advanced materials emulating the well-known super-hydrophobic effect of the lotus leaf[124] and adhesive surfaces of the gecko's feet.[125] Structural colours and iridescence are most often observed in invertebrates such as butterflies (see Figure 9) and beetles, but also in the feathers of birds.[128,129] Since the early observations of functional nanostructures in nature, engineers have tried to replicate these nanostructures in order to functionalize surfaces.[130–132] Recently, Christiansen et al.[127] developed a surface consisting of 1D gratings with varying wave length and orientation, resulting in a glitter colour effect, where the colour appearance is angle dependent, see Figure 9(a). The nanostructures are in first place created in a clean room, where technologies from the
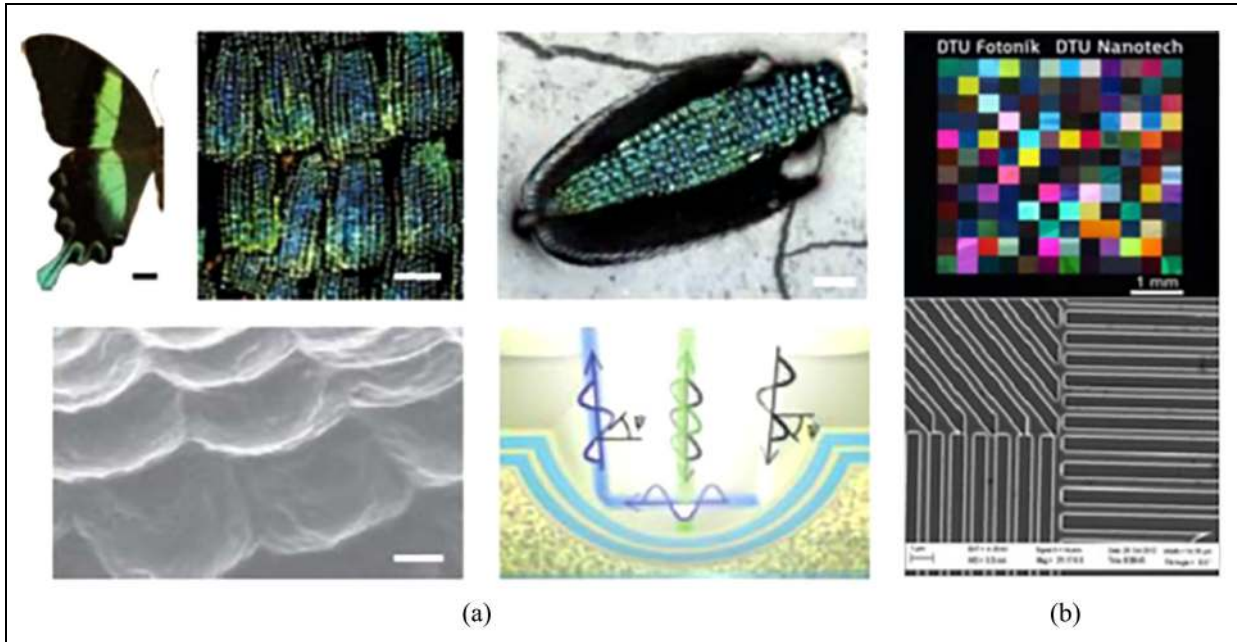
Figure 9. (a) Green swallowtail, an explanation of colours.[126] (b) Diffraction gratings with different orientations and periods can be combined, resulting in a glitter colour effect.[127]

semiconductor industry, such as electron beam lithography (EBL) and standard ultraviolet (UV)) lithography, are applied in order to transfer the nanostructures to a silicon wafer. From there, the nanostructures are transferred to the surface of the material where the functionality is wanted via a technology called NIL a technology invented in 1995.[133]

In the study conducted by Sonne et al.,[134] the objective was to upgrade existing injection moulding production technology for manufacture of plastic components by enhancing the lateral resolution on free-form surfaces down to micrometre and nanometre length scales. This will be achieved through the development of a complete NIL solution for structuring the free-form surface of injection moulding tools and tool inserts. This will enable a cost-effective and flexible nanoscale manufacturing process that can easily be integrated with conventional mass production lines. The proposed technology enables functionality of plastic surfaces by topography instead of chemistry with some of the applications as describe above (e.g. colour or hydrophobic effects). A manufacturing process resembling some of the same methods as presented here, though with a nickel foil used for transferring the nanostructures, has been shown in the literature.[134–136] Furthermore, other manufacturing processes associated with additive manufacturing (AM) such as direct laser writing (DLW) allow for creating sub-100 nm structures with similar functionalities as mentioned above.[137] However, the method presented in this work allows for resolutions as achieved in the semiconductor industry and the wafer-

based platform makes the process competitive to the AM methods in a mass production environment. The anticipated pattern transfer method from a silicon wafer to final injection moulded plastic product is visualized in Figure 10 (this technology has been tested at pilot scale and implemented industrially[138]). (1) A planar microstructured and nanostructured master is prepared by existing microfabrication and nanofabrication techniques such as EBL and photolithography. (2) A flexible stamp is designed, replicated from the planar master. (3) The injection moulding tool insert is coated with a polymer resist for NIL. (4) Stamping equipment is employed to imprint the flexible stamp (by a blow-moulding like process) into the double curved (free-form) injection moulding tool insert by use of compressed air. The flexible stamp is imprinted into the resist on the insert. (5) The injection moulding tool insert surface is patterned by means of electroplating or etching, using the imprinted polymer resist as a masking layer. (6) The nanostructured injection moulding tool insert is used in a conventional injection moulding process.

For NIL on injection moulding tool inserts (and on double curved surfaces in general), the deformation and stretch of the flexible stamp can be up to 50% and in the millimetre range.[139] This is problematic since even very small changes in the nanostructures geometry will change the wanted overall functionality.[140] The deformations are therefore important to take into account, when the planar silicon masters are designed. Here simulation tool such as the finite element method
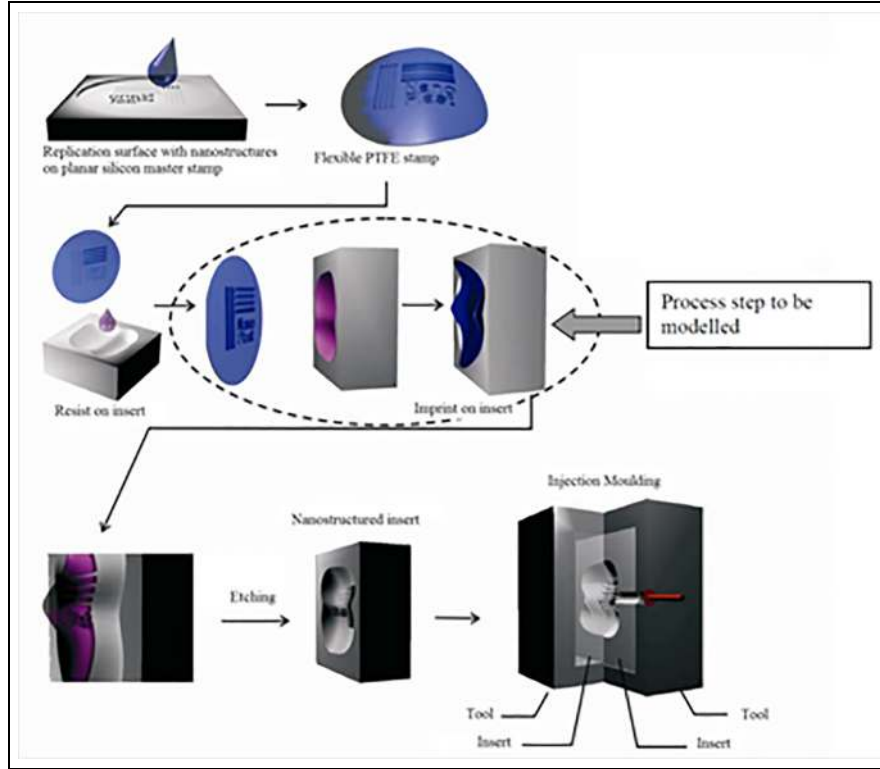
Figure 10. A flexible nanoimprint solution for nanostructuring an injection moulding tool insert.[130]

(FEM) is an appropriate way of predicting those deformations. Numerical models for simulating the NIL process in general have been shown in the literature,[141–144] with the main purpose of solving for the flow of resist and the local stamp bending, with the classical squeeze flow model (the Stefan equation[145]) as benchmark

$$\frac{1}{h^2} = \frac{1}{h_0^2} + \frac{2p}{\eta s^2} \qquad (20)$$

where h is the height of the resist, p is the pressure, η is the viscosity and s is the permeability.

The Stefan equation is however not directly suitable for the NIL on curved surfaces due to a number of different aspects that complicates the overall physics: (1) Because of the large deformations and hence strains in the flexible stamp, non-linear geometry has to be taken into account in order to get accurate results from the numerical simulations.[146] (2) The material behaviour is non-linear and is for the polymer material described by a viscoelastic–viscoplastic constitutive behaviour.[147,148] (3) With respect to the contact conditions, changes in frictional behaviour on the different length scales (macroscale to nanoscale) have to be taken into account[149–152] and add yet another nonlinearity to the system of equations that have to be solved. Here, multiscale modelling is an approach where the global and local conditions can be taken into account in the same model.[153]

In the work done by Sonne et al.[134] a standard continuum mechanics was applied with the overall goal of solving the three static equilibrium equation

$$\sigma_{ij,i} + p_j = 0 \qquad (21)$$

where p_j is the body force at any point within the geometry and σ_{ij} is the stress tensor. The flexible stamp is in this case made of polytetrafluoroethylene (PTFE) which due to its thermal resistance is suitable for NIL which normally is performed at elevated temperatures (when applying a non-UV curing resist). The material behaviour has to a large extend been shown in the literature, and different corresponding constitutive models have been proposed[154–156] These different contributions are in overall agreement on how the PTFE material by a 1D rheological representation can be described. In the present work, the overall approach is to include the viscoelastic behaviour represented by a Zener body[155] by a modified version of Hooke's law represented by the elastic stiffness tensor

$$C_{ijkl}^{\mathbf{ve}} = \frac{E_{\mathrm{mod}}}{1 + \nu}\left[\frac{1}{2}\left(\delta_{ik}\delta_{jl} + \delta_{il}\delta_{jk}\right) + \frac{\nu}{1 - 2\nu}\delta_{ij}\delta_{kl}\right] \qquad (22)$$

$$E_{\mathrm{mod}} = E_{\mathrm{max}} + E_2, \ \ E_{\mathrm{max}} = \frac{E_1}{\frac{E_1\Delta t}{\eta} + 1} \qquad (23)$$

where η is the viscosity of the dashpot, E_1 and E_2 are Young's moduli for the springs and Δt is the time
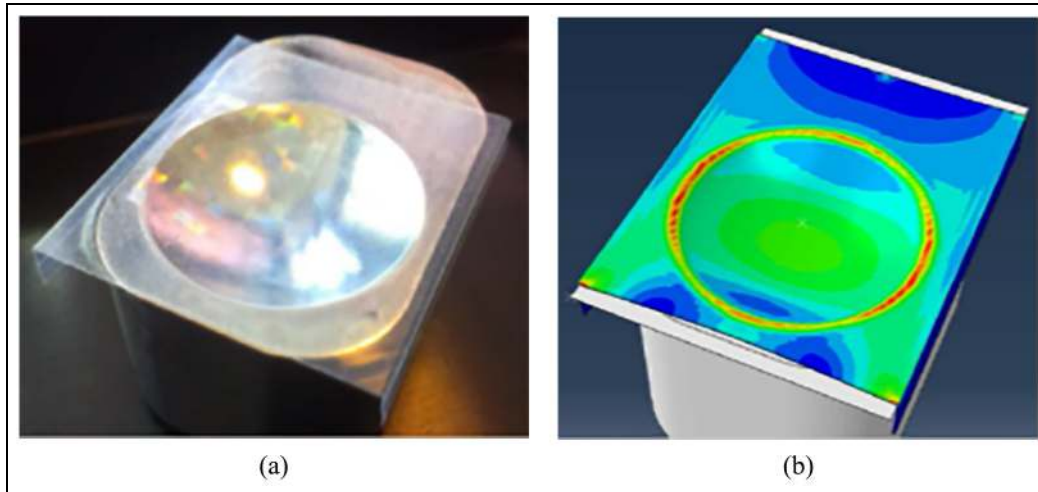
Figure 11. (a) The used flexible stamps with the glitter effect nanostructure on top of the steel tool insert after nanoimprint. (b) Numerical model of the same setup where it is possible to study the strain field within the flexible stamp in combination with the actual imprinting pressure underneath the flexible stamp.[130]

increment size. It is assumed that J_2 flow theory applies during the viscoplastic deformation of the PTFE material. Hence, the material has to satisfy the von Mises yield condition

$$f = \sigma_e^2 - \sigma_y^2 = 0 \qquad (24)$$

where σ_e is the equivalent stress. The yield stress σ_y is in this work given by the J-C viscoplastic model,[157] which from previous work has been shown to give a reasonable correlation between strain, strain rate, temperature and stresses for this material.[158]

The model has been verified through a series of experiments, where NIL on a double curved tool insert for injection moulding (Figure 11(a)) was performed with different process parameters. The outcome of the model is first of all contour plots of the maximum principal strain field on the geometry of the deformed flexible stamp (see Figure 11(b)). This will give an indication of how much the nanostructures have been stretched during the nanoimprinting process. Furthermore, the transient pressure distribution between the mould and flexible stamp can be examined and used to optimize the process parameters in terms of imprinting temperatures and pressures and the thickness of the flexible stamp.

For the application shown in Figure 11, good agreement between simulations and experimental results in terms of maximum principal strain was found, see Figure 12.

In general, both experiments and simulations have shown a mismatch between the defined and measured nanostructures as a result of stretching of the flexible stamp. This clearly indicates the necessity for numerical models in order to take this deformation into account
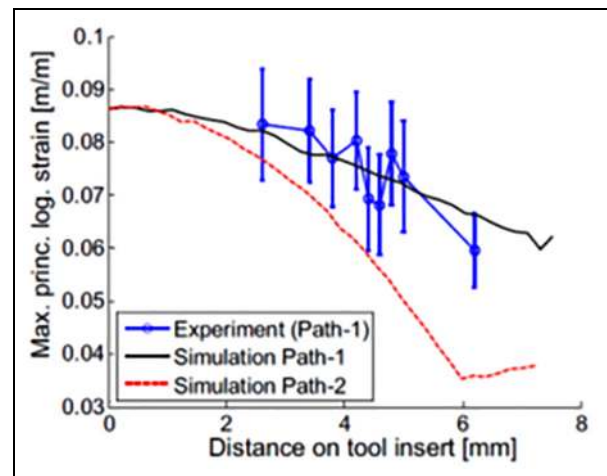
Figure 12. Comparison of measured and calculated maximum principal strains along two different paths on the deformed flexible stamp.[130]

when the nanostructures are designed in the first step of the process. The developed models have shown to predict the stretch of the nanostructures with a maximum error of 0.5% defined as the difference between measured and simulated wave lengths of the nanostructures on the surface of the deformed flexible stamp,[130] indicating their ability to capture the essential physics of this manufacturing process.

Modelling manufacturing of composites

Fibre-reinforced polymer (FRP) matrix composite materials have found widespread use in the manufacture of large energy critical structural applications such
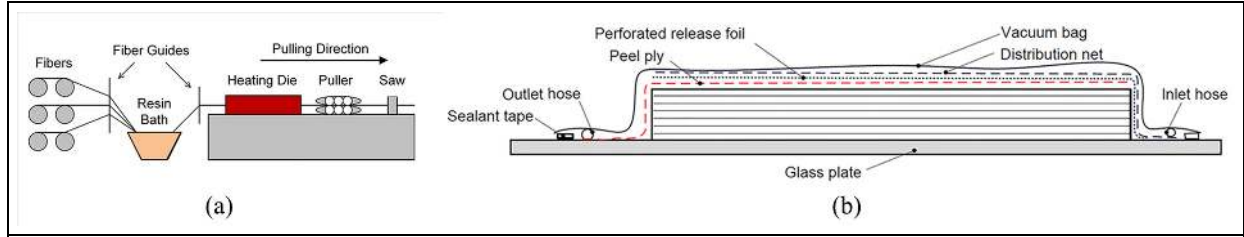
Figure 13. (a) Schematic view of the traditional pultrusion process and (b) schematic illustration of VARTM.

as wind turbine blades where low weight and high strength are crucial. In the wind energy industry, the use of FRP composites in large wind turbine blades has surpassed all other materials for both the load-carrying and airfoil sections of the blades.[159] Composites offer a low weight-to-stiffness ratio and user-defined high durability and strength. Application-defined properties are also more readily obtained by tailoring the composite lay-up, thicknesses and fibre/matrix combinations according to the mechanical, thermal, electrical or aesthetic requirements. During the manufacture of thermoset polymer composites in general, the reinforcement fibre material is moulded into a desired shape by impregnation and curing of the fibres with a liquid polymer resin, typically a thermosetting epoxy or polyester. Upon curing a structural unified solid combination of these materials is achieved, resembling the mould geometry. Many different variations of this basic process exist, for instance pultrusion,[160,161] filament winding,[162,163] resin transfer moulding (RTM),[164–166] vacuum infusion (VI),[167] vacuum-assisted resin transfer moulding (VARTM),[168] to name a few.[169] In this article, focus is on two different processing methods: pultrusion and VARTM, see Figures 13(a) and (b), respectively. The combination of thick geometries, cure cycles at elevated temperatures and the highly non-linear resin phase transition characteristics and release of latent heat can make the process complex to control.[170–172] Furthermore, avoiding process-induced shape distortions and residual stress build-up remains a challenge in many applications.[173]

Only the main features of the needed theory for modelling of composite manufacturing will be outlined here. In order to analyse the thermal conditions during processing, the energy equation must be solved

$$\rho c_p \left(\frac{\partial T}{\partial t} + u \frac{\partial T}{\partial x} \right) = k_x \left(\frac{\partial^2 T}{\partial x^2} \right) + k_y \left(\frac{\partial^2 T}{\partial y^2} \right) + k_z \left(\frac{\partial^2 T}{\partial z^2} \right) + \dot{Q}''' \tag{25}$$

Note here that the material flow during processing is taken into account via the advection on the left-hand side, where u is the pulling speed in the x-direction for

pultrusion, and $u = 0$ for VARTM. Other material flow than this is not considered here. $\dot{Q}'''$ is determined by the total reaction enthalpy of the matrix material and the cure rate which in turn depends on the degree of cure and temperature in a highly non-linear manner, often described by the Kamal and Sourour autocatalytic kinetic expression.

Thermoset resins also exhibit volumetric shrinkage during curing, sometimes as high as 9% for polyesters. Moreover, as the resin develops from the viscous state to the solid state, large changes in the thermal and mechanical properties occur. Johnston[174] proposed a modified linear elastic model incorporating temperature dependency which also allows thermal softening.[171,175,176] This model which is often denoted the model cure hardening instantaneous linear elastic (CHILE) model is used in the present work. This indicates that with an increase in degree of cure, the modulus increases monotonically. User-defined subroutines are developed in ABAQUS for the constitutive material models. The corresponding expression for the CHILE model is seen in equation (26)[177]

$$E_r = \begin{cases} E_0 & ; \quad T^* \leq T_{C1} \\ A_e \exp(K_e T^*) & ; \quad T_{C1} < T^* < T_{C2} \\ E_1 + \dfrac{T^* - T_{C2}}{T_{C3} - T_{C2}} (E_\infty - E_1) & ; \quad T_{C2} < T^* < T_{C3} \\ E_\infty & ; \quad T_{C3} \leq T^* \end{cases} \tag{26}$$

where T^* represents the difference between the instantaneous glass transition temperature (T_g) and the resin temperature T, that is, $T^* = T_g - T$. A_e and K_e are the constants for the exponential term. T_{C1}, T_{C2} and T_{C3} are defined as the critical temperatures and E_0, E_1 and E_∞ are the corresponding elastic modulus values, respectively. More specifically, E_0 and E_∞ are the viscous and glassy state elastic modulus, respectively. T_g can be defined as

$$T_g = T_g^0 + a_{T_g} \cdot \alpha \tag{27}$$

where T_g^0 is the glass transition temperature at $\alpha = 0$ and a_{T_g} is a fitting constant.
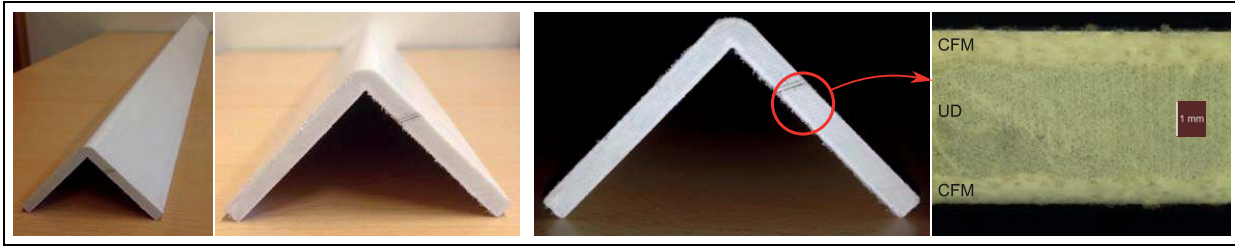
Figure 14. Pultruded L-profile.[119]

The effective mechanical properties as well as thermal and chemical shrinkage strains of a laminate are calculated using a micromechanics approach, for example, the self consistent field micromechanics (SCFM) approach which is a well-known and documented technique in the literature.[178]

During composites processing, manufacturing-induced strains are known to develop as a result of the matrix material chemical cure shrinkage in combination with thermal gradients as well as mismatch in thermal expansion properties.[179] More specifically, knowing the isotropic resin shrinkage strain, the incremental longitudinal and transverse chemically induced shrinkage can be determined for a composite material taking micromechanics into account. Thermal strain increments are calculated in a similar manner based on the temperature change and the composite effective thermal expansion coefficient. Since strains are in general small, linear strain decomposition can be used such that the process-induced strains are expressed as the sum of the thermal strains and chemical strains and finally the total strains are hereafter found from adding the mechanical strains and process-induced strains. At each time step, the properties of the rein are updated. Using the SCFM approach, the effective properties of the composite laminate are then calculated in which the fibre properties are assumed to remain constant.[180]

### Numerical modelling of pultrusion

Pultrusion is a cost-effective production process for manufacturing FRP composite profiles. Constant cross-sectional profiles are produced in a continuous manner. The resin material impregnated the fibre reinforcements in a resin bath system while being pulled by a pulling mechanism. Curing takes place inside the heater pultrusion die. A saw is often used to cut the profile into desired length. A schematic illustration of the process is seen in Figure 13.

Pultrusion process has been analysed using various thermo-chemical numerical models since 1980s in order to control the curing and temperature distribution during processing.[181,182] Some of the thermo-chemical computational analyses can be found in previous works.[183–188]

Baran et al.[119,189,190] have made the first thermo-chemical-mechanical model of pultrusion in which a coupled thermo-chemical-mechanical is developed using ABAQUS and used to model the pultrusion of the L-shaped profile as shown in Figures 14 and 15. In Baran et al.,[191] a more comprehensive mechanical model was proposed to analyse the process in 3D by calculating the stresses and shape deformation. A glass/polyester was considered in Baran et al.[119] for the UD as well as the CFM layers, and for the die, a chrome steel was used. As shown in Figure 15, the heating regions were 275 mm long and 60 mm wide and they were placed 150 mm apart from each other. The length of the die was 1000 mm and the post-die region was 5000 mm long. The surfaces of the composite at the post-die region were exposed to convective cooling boundary condition. Similar boundaries were also defined for the die surfaces except the heater regions. The polyester resin entering the die inlet was assumed to be at uncured viscous state and the curing took place with the help of heaters. The necessary material properties were characterized in Baran et al.[177] such as curing kinetics, temperature and cure-dependent elastic modulus and viscosity.

The generalized plane strain elements CPEG8R available in ABAQUS were used in the 2D quasi-static mechanical analysis. Figure 15 shows the 2D cross-section of the L-shaped profile. A Lagrangian framework was applied in the 2D mechanical model such that the temperature and cure distributions calculated in the 3D thermo-chemical model as well as the mechanical boundary conditions were updated at each quasi-static time step.[192] The model predicted the stress–strain development as well as the nodal displacements.[192]

The predicted spring-in angle as a function of the pulling distance is depicted in Figure 16 (left). It is seen that the deformation process of the profile continues until around 6 m away from the die-exit during the cooling stage in air. The final spring-in angle as a function of different pulling speeds from 500 to 1000 mm/min is depicted in Figure 16 (right). It was found that the spring-in angle increased with pulling speed. Moreover, the final spring-in for parts produced with a pulling speed of 600 mm/min was measured and good agreement with the predicted value was found.
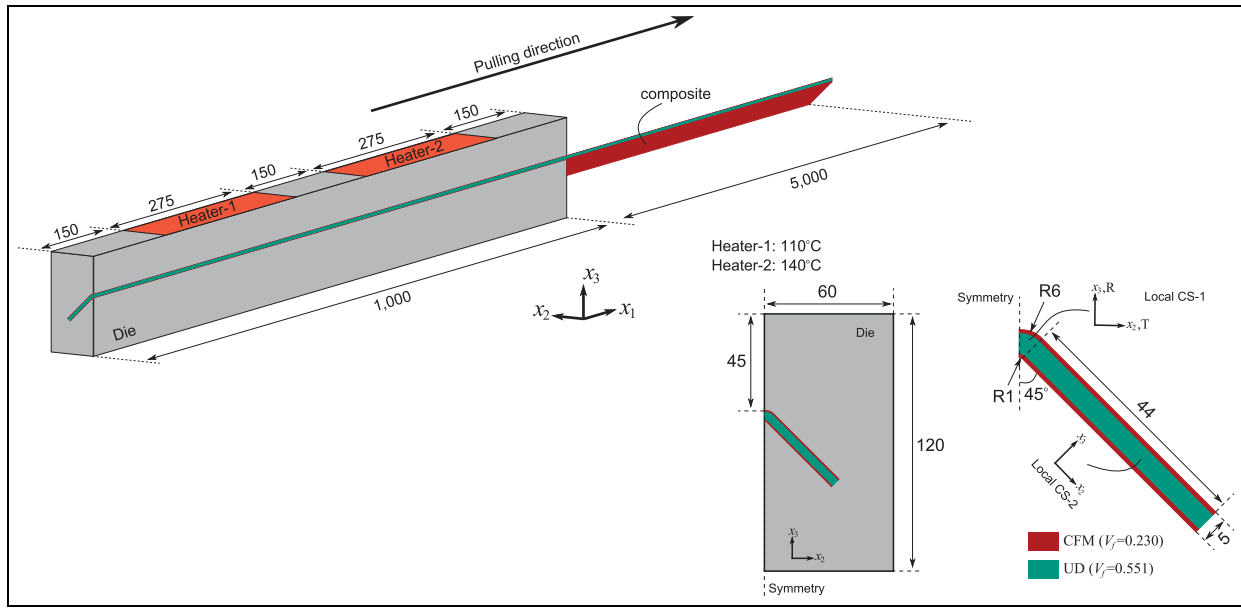
Figure 15. Pultrusion setup of L-shaped profile with dimensions indicated.[119]

In Baran,[193] the process-induced residual stress development was described for a 100×100 mm pultruded square profile made of glass/polyester. The temperature and degree of cure distributions were calculated for three different preheating temperatures. The nonuniform internal constraints in the part yielded in an internal shear deformation during the process. The transverse shear stress and compressive normal stress levels decreased significantly as compared with the tensile normal stresses with an increase in preheating temperature. Predicted transverse shear stress distributions are depicted in Figure 17.

The mechanical properties of the fibre-reinforced composite materials might vary significantly due to the manufacturing-induced effects.[194] The possible causes for this variation can be the nonuniform distribution of fibre/matrix, fibre misalignment, residual stresses at micro and meso level, dry spots and voids due to poor impregnation and so on. The probabilistic and reliability analyses of the pultrusion process were studied in Baran et al.[195,196] The variability in the product properties and their effects on the curing and temperature were investigated. In addition, the process conditions were optimized in several studies for the pultrusion process.[197–200]

Modelling process-induced strains and stresses in a thick laminate plate

The internal strain development during curing of a thick laminate plate at elevated temperatures using a long cure cycle was analysed by Nielsen et al.[175,176] The objective with the study was to evaluate how accurate

the aforementioned CHILE constitutive model is at predicting the internal strain development, in what is essentially a viscoelastic problem. 3D numerical model total strain predictions are compared with experimentally determined in situ strains within the laminate part, using embedded optical fibres with fibre Bragg grating (FBG) sensors. Hence, a direct comparison can be made with model predictions, capturing how thermal expansion and chemical shrinkage strains develop within the laminate throughout curing during the VI moulding process, as well as the influence of tooling.

A glass/epoxy UD laminate was manufactured using the VI techniques. The dimension of the laminate was 400×600 mm consisting of 52-layer UD E-glass fibre mats. A tempered glass of 10 mm thickness was employed as a mould.[175,176] Prior to infusion, sensors were embedded within the dry preform; including thermocouples and optical fibres (FBGTop, FBGCenter and FBGBottom), each consisting of three FBG sensors interspaced along the optical fibre, see Figure 18(a). The optical fibres were placed transversely to the main reinforcement fibre direction in order to capture the matrix-driven process strains. The laminate was vacuum infused and cured at 40°C on a heated plate.

A sequentially coupled thermomechanical numerical analysis was subsequently conducted. Symmetry conditions were assumed why only half of the laminate plate and tool was modelled (Figure 18(b)). In the thermal step, Dirichlet boundary conditions (known temperatures) were prescribed on the laminate plate top and bottom surfaces, as determined experimentally. Moreover, the heat flux through the symmetry plane was neglected. In the mechanical step, a tied condition
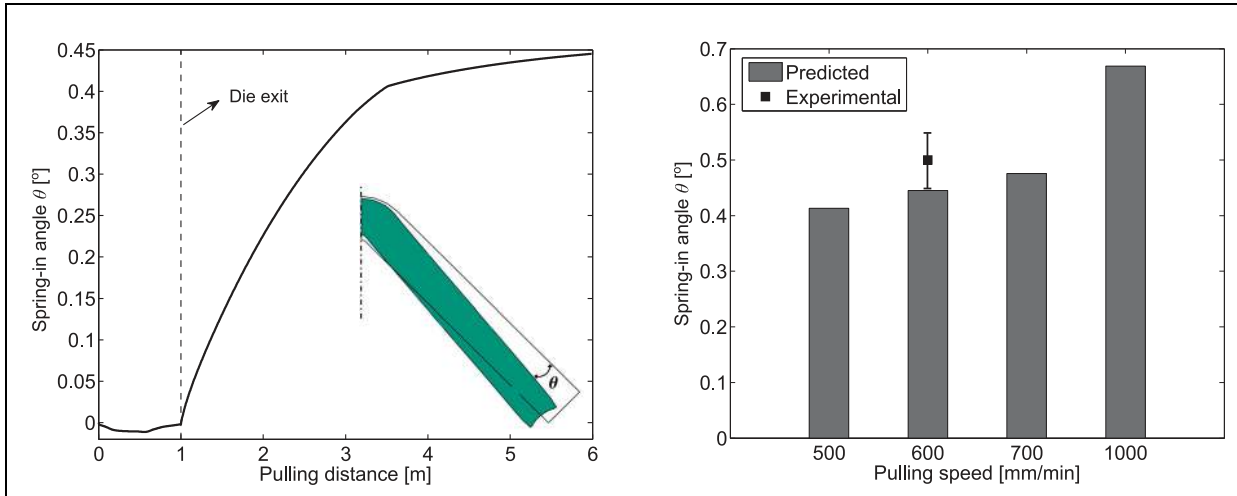
Figure 16. Left: Predicted spring-in angle of L-shaped profile as a function of the pulling distance. Right: Predicted spring-in angles for different pulling speeds (compared with experimentally found value for 600 mm/min[119]).
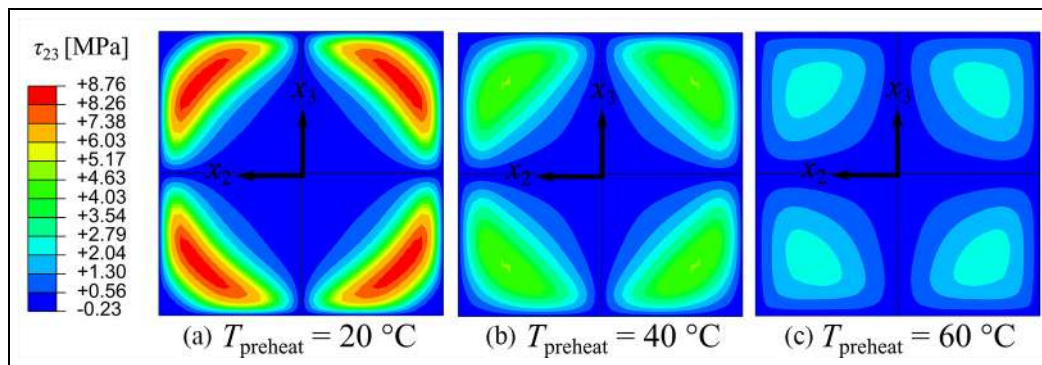
Figure 17. Transverse shear stress distribution (τ_{23}) for different $T_{preheat}$ values after the pultrusion process.[193]
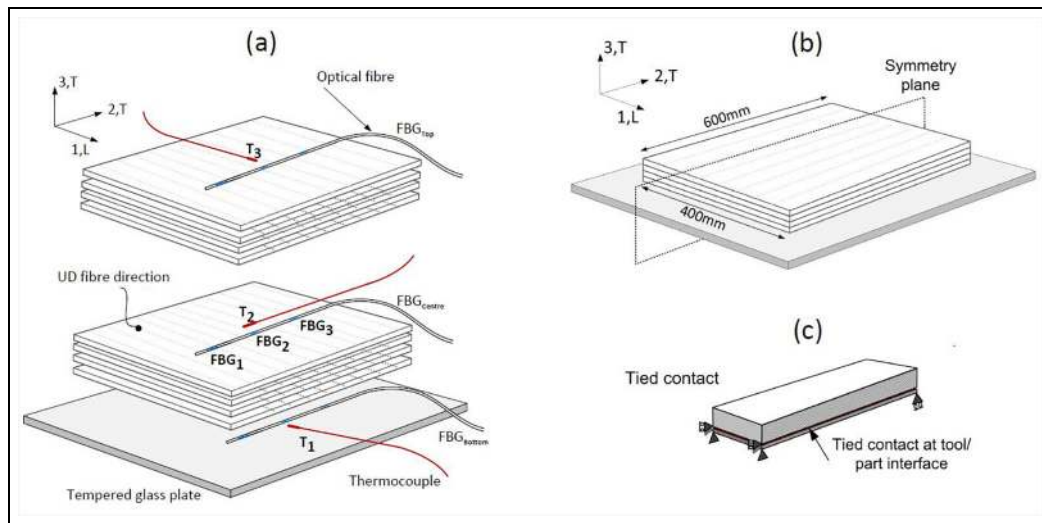
Figure 18. Schematic of (a) exploded view showing the embedded sensor placement, (b) laminate and tool plane of symmetry and (c) mechanical contact conditions assumed.[175]
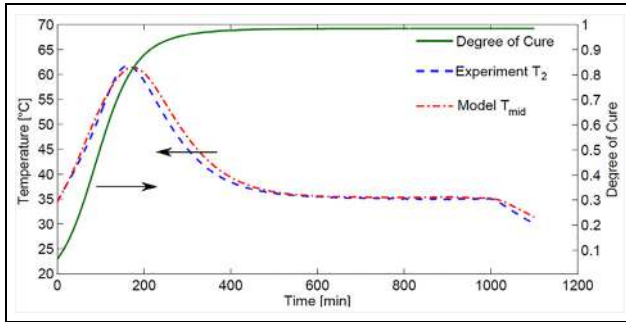
Figure 19. Experimental laminate mid-plane temperature and model prediction. Also shown is the corresponding modelled cure degree development.[171]

Figure 20. Process-induced total transverse strain comparison between model predictions and experimental data. Also seen is the predicted cure degree development at the laminate plate centre.[171]

at the tool/part interface was prescribed, mimicking perfect bonding between the tool and laminate during the process. This condition is a simplification of real-life sliding, sticking and other cohesive interfacial contact conditions. In the model, it was assumed that the preform is perfectly impregnated through the use of a constant fibre volume fraction resembling the final state of the part after processing.[171] Demoulding is modelled after curing at ambient temperature by simply suppressing all mechanical constraints between tool and part.

Figure 19 presents the experimentally determined centre plane laminate temperature (T2), compared with model predictions of temperature and corresponding cure degree model predictions. Upon commencement of the curing reaction, an increase in temperature is seen as a result of heat generation during the release of latent heat upon matrix cross-linking. After the temperature peak, a steady-state temperature is upheld corresponding to approximately 40°C, after which the laminate cools to ambient temperature. It is seen that a substantial amount of curing develops prior to when the exothermic peak temperature is reached. This relates to the autocatalytic equation for the cure rate being self-catalysed by increases in temperature.[171]

Figure 20 shows the comparison of the predicted transverse strains with the measured ones at the centre of the laminate (mid-plane). The total strains are seen to relate somewhat to the thermal profile presented in Figure 19, deferring mainly due to the influence of chemical cure shrinkage. Good agreement between the model predictions and the experimentally measured strains is observed, with the best agreement early in the process. As the resin cures, the strain development goes from being driven by the tool expansion due to the tied contact, to being driven by the induced thermal and chemical shrinkage laminate strains.

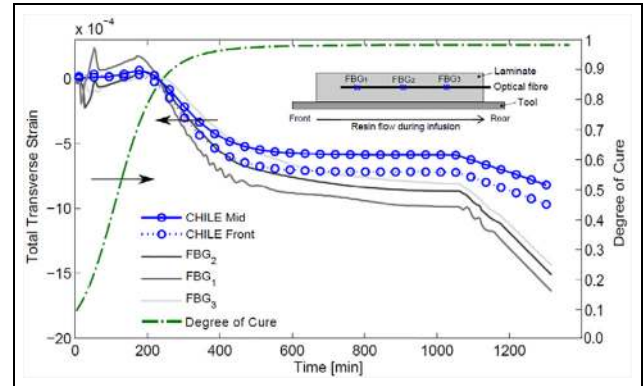The influence of the tool (tempered glass plate) is visible upon cooling, that is, at time of 1050–1300 min. It is seen that a smaller gradient is present on the

predicted total strain curves as compared to the experimentally determined strains. This may be due to the lower coefficient of thermal expansion (CTE) of the tempered glass plate ($9.0 \times 10^{6}°C^{-1}$) as compared with the transverse CTE of the laminate plate in the glassy (cured) state ($46.07 \times 10^{6}°C^{-1}$). The tool–part interaction may cause the difference in strain between the model and experiments during cooling down stage, for example, stick–slip friction contact behaviour. In order to accurately model this behaviour at the tool/part interface, information of contact properties such as the orthotropic friction coefficients, along with the maximum effective contact shear stress, is needed, as a function of temperature and cure degree. Hence, the tied contact approximation is a reliable simple representation.

Thermo-metallurgical modelling of SLM

Modelling of thermal conditions during manufacturing processes and resultant metallurgical features is a well-established field of research.[201–208] In the case of SLM, however, the application of these techniques of microstructure predictions is still limited. Nonetheless, the plethora of experimental studies in the literature focusing on characterizing and empirically predicting the microstructure during SLM of materials[209–212] clearly indicates the scope and need of thermo-metallurgical modelling studies.[213,214] In this section, a brief overview of the work carried out on thermo-metallurgical modelling of SLM is presented. Subsequent to a brief outlining of the theory associated with the thermo-metallurgical model, the evolution of centre-line microstructure during single melt track formation is simulated and discussed.

SLM[215] process was developed in Fraunhofer Institute for Laser Technology in Aachen, Germany

and it has since been a prominent centre for research in SLM. Together with selective laser sintering and electron beam melting, it is among the most prevalent form of metal AM. Potential target areas providing significant scope for SLM include aerospace applications, automobiles and medical implants. Due to the clear advantages of such an AM process, SLM has been the subject of intense research in the last decade. SLM and similar metal AM processes have been reviewed in previous works[216–224] from experimental and modelling perspective, including current practices and future challenges regarding raw materials, processing and postprocessing.

The SLM process begins after a sliced 3D CAD model is received by the machine. The sliced model contains information about the zones to be melted in different layers. A powder scrapper moves some powdered material from the feed container onto the build platform, distributing it more or less uniformly. Then the laser beam source is turned on. Typically, a Nd:YAG or CO_2 laser having a Gaussian energy distribution is used as a power source for selectively melting certain zones in a layer of powdered material, which eventually give rise to a 3D structure (Figure 21). The generated beam is deflected by scanner mirrors which control the movement of the laser beam over the powder surface. The beam is focused by the help of a lens that can alter the focusing distance and the divergence of the beam. Depending on the input from the sliced 3D model, the laser beam melts out a shape in the powder layer. Upon completion of the laser treatment, the build platform moves down by a fixed amount and another layer of powder is scrapped onto it. The process is repeated until

the complete 3D object is created. The entire process is carried out in an inert atmosphere of argon or N_2 with continuous gas flow through the chamber.

In SLM process, the melt pool size (typically in the range of 100–500 μm) is small enough compared to the size of the component being manufactured that conduction becomes the primary mode of heat transfer in the entire domain. In such a case, the spatial and temporal distribution of temperature is governed by the heat conduction equation, which can be expressed as

$$\rho C_p \frac{\partial T}{\partial t} = \frac{\partial}{\partial x}\left(k_{xx}\frac{\partial T}{\partial x}\right)$$
$$+ \frac{\partial}{\partial y}\left(k_{yy}\frac{\partial T}{\partial y}\right) + \frac{\partial}{\partial z}\left(k_{zz}\frac{\partial T}{\partial z}\right) + \dddot{\Phi} \quad (28)$$

where T is the temperature, t is the time, (x, y, z) are the spatial co-ordinates, k_{xx}, k_{yy} and k_{zz} are the thermal conductivities in the different directions, ρ is the density, C_p is the specific heat and $\dddot{\Phi}$ is the heat source term. However, at a local scale, several interacting physical phenomena such as Marangoni flow in the melt pool, keyhole formation and vapour expulsion, inter-particle radiative heat transfer, temporary plasma formation and collapse can occur depending upon the process parameters. Using a conductive heat transfer based model to simulate the SLM process, thus, requires several modifications and calculation of equivalent material properties. For instance, SLM is usually carried out in a chemically inert gaseous environment under continuous flow, which can be modelled via a thermal interaction at the components exterior boundaries following the Newtonian cooling and Stefan–Boltzmann law

$$-k\frac{\partial T}{\partial \eta} = -h(T_{\text{amb}} - T) + \sigma\varepsilon(T^4 - T_{\text{amb}}^4) \quad (29)$$

where h is the heat transfer coefficient, T_{amb} is the temperature of the gaseous environment, σ is the Stefan–Boltzmann constant and ε is the emissivity of the material. The above thermal equations can then be solved using any of the different numerical techniques.[226–230]

One of the most common material property for which an equivalent value is required when using a conductive heat transfer formulation is the emissivity of the powder bed. The current work is based on the predictive models proposed by Sih and Barlow[231–233] wherein a combination of the emissivity of the particles and the emissivity of the cavities in the powder bed is used

$$\varepsilon = A_h\varepsilon_h + (1 - A_h)\varepsilon_s \quad (30)$$

where ε is the effective emissivity of the powder bed, ε_s is the emissivity of the bulk material, ε_h is the emissivity of the cavities and A_h is the area fraction of surface
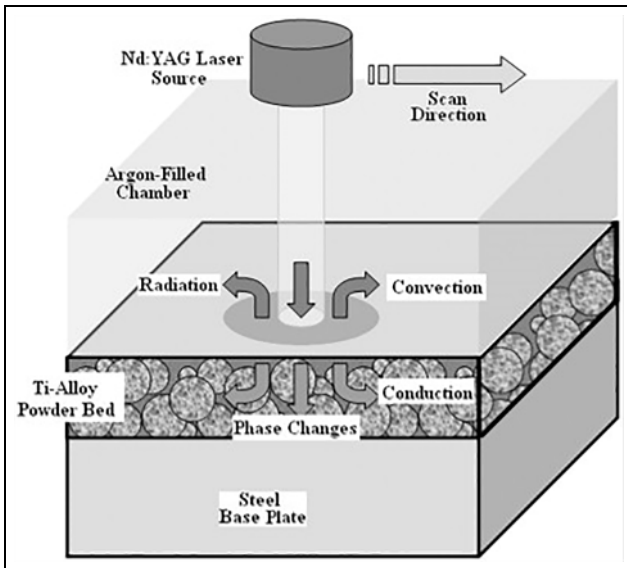
Figure 21. Schematic representation of heat transfer during selective laser melting.[225]

occupied by the cavities. The morphology as well as density of the powder bed packing influences the effective emissivity via the area fraction, A_h. For a randomly packed powder bed of porosity (ϕ), the area fraction and the emissivity of the cavities are given by

$$A_h = \frac{0.908\phi_0^2}{1.908\phi_0^2 - 2\phi_0 + 1} \tag{31}$$

$$\varepsilon_h = \frac{\varepsilon_s\left[2 + 3.082\left(\frac{1-\phi_0}{\phi_0}\right)^2\right]}{\varepsilon_s\left[1 + 3.082\left(\frac{1-\phi_0}{\phi_0}\right)^2\right] + 1} \tag{32}$$

Similarly, effective thermal conductivity values also need to be found for the powder bed as well as for molten/vaporized materials. A modified version of the Zehner–Schlünder–Damköhler model found in the literature, which describes a randomly packed powder bed formed of mono-sized spherical powder particles, can be used to calculate the equivalent thermal conductivity as

$$\begin{aligned}
\frac{k}{k_f} &= \left(1 - \sqrt{1-\phi_0}\right)\left(1 + \phi_0\frac{k_r}{k_f}\right) \\
&+ \sqrt{1-\phi_0}\left(\frac{2}{1-\frac{k_f}{k_s}}\left(\frac{1}{1-\frac{k_f}{k_s}}\ln\left(\frac{k_s}{k_f}\right) - 1\right) + \frac{k_r}{k_f}\right)
\end{aligned} \tag{33}$$

where k is the effective thermal conductivity of the powder bed, ϕ_0 is the porosity of the powder bed, k_s is the thermal conductivity of the bulk material, k_f is the thermal conductivity of the gaseous environment and k_r is the equivalent thermal conductivity arising due to interparticle radiation given by

$$k_r = 4F\varepsilon\sigma_B T_p^3 D_p \tag{34}$$

where σ_B is the Stefan–Boltzmann constant, T is the mean absolute temperature and D_p is the diameter of powder particles. F is called the view factor and can be chosen as a function of the emissivity of the powder bed leading to

$$k_r = \frac{4\varepsilon\sigma_B T_p^3 D_p}{1 - 0.132\varepsilon} \tag{35}$$

Similarly, for properties related to laser–material interaction such as albedo, scattering coefficient, extinction coefficient, equivalent values need to be calculated. While the involved physics can typically only be modelled via differential and integral equations, simple empirical models drawing upon experimental results do exist in the literature. For instance, the extinction coefficient (α) and scattering albedo (ω) of bulk material can be used to approximate an effective absorption coefficient for the powder bed with an assumption of diffusive reflections on powder particles[228]

$$A^{\text{effective}} = \frac{3}{4}\left(\frac{1 - \omega + 3\alpha}{1 + 2\alpha}\right) \tag{36}$$

$$\alpha = \left(1 - \frac{2}{3}\omega + \frac{1}{3}\omega^2\right)^{\frac{1}{2}} \tag{37}$$

Apart from calculation of equivalent material properties, the heat conduction equation also needs to be provided with appropriate heat source term $\overset{\cdots}{\Phi}$ in order to account for heat input via the laser beam. In case of a simple laser beam with a Gaussian distribution profile, the irradiance is given by

$$I(x,y) = \frac{2\alpha P_0}{\pi\omega_0^2}e^{-\left[\frac{2\left((x-x_0)^2 + (y-y_0)^2\right)}{\omega_0^2}\right]} \tag{38}$$

where P_0 is the power of the laser beam, ω_0 is the beam $1/e^2$ radius and α is the absorptivity of the laser beam in the material. For a laser beam moving on the powder bed with a velocity (v_x, v_y), the thermal flux is thus computed as

$$\begin{aligned}
q_s(x,y) &= \frac{2\alpha P_0}{\pi\omega_0^2} \\
&\times \iiint e^{-\left[\frac{2\left((x-x_0-v_xt)^2 + (y-y_0-v_yt)^2\right)}{\omega_0^2}\right]}dxdydt
\end{aligned} \tag{39}$$

where q_s is the thermal flux, (x_0, y_0) is the initial location of the laser beam and t is the time. The calculated thermal flux then needs to be converted into an equivalent volumetric heat generation to be put into the heat conduction equation as a source term. The above governing equations and constitutive models are sufficient to develop a continuum model of the thermal conditions during SLM.[228,230,234–237]

The internal state variable approach[238] is well suited to the development of models for non-isothermal microstructural evolution. In general, a microstructure may be defined by different state variables such as grain size, volume fraction of grains, fraction of solid in solidification. For the current case of solidification, two internal state variables can be used to describe the microstructure evolution – namely temperature and fraction of solid. The usage of these two state variables for modelling solidification microstructure is described below.

The interaction of the two state variables (temperature and fraction of solid) determines the type of microstructure formed during solidification. All grains produced during solidification are assumed to be equiaxed in nature, with columnar grains considered to be similar to elongated equiaxed grain.

The equiaxed solidification begins with nucleation in the regions of melt pool just below liquidus temperature and along the boundary of the melt pool. Although nucleation is a randomized phenomenon, statistical models exist for characterizing the overall nucleation in a melt pool. The Oldfield model[239] is most popular wherein the nucleation distribution is described by a Gaussian distribution. The grain density at a particular undercooling is given by

$$
\begin{aligned}
n(\Delta T) = &\int\limits_{0}^{\Delta T} \frac{n_{max}}{\Delta T_{\sigma}\sqrt{2\pi}} \\
&\exp\left[-\frac{1}{2}\left(\frac{\Delta T'-\Delta T_N}{\Delta T_{\sigma}}\right)^2\right]d\Delta T'
\end{aligned}
\tag{40}
$$

where n_{max} is the maximum possible nucleation density, ΔT_N is the mean undercooling and ΔT_{σ} is the standard deviation of the grain density distribution. Typically, these three parameters need to be obtained experimentally for a given material and condition.

Nucleation can occur in a homogeneous or heterogeneous manner; however, the latter is much more common due to less energy requirements. The heterogeneous nucleation in the above model is assumed to be instantaneous and dependent on the characteristic undercooling. Once nucleated, the grains start to grow outwards. This results in the fraction of solid in the local melt pool area increasing, and there is corresponding release of latent heat of fusion which might increase the local temperature(this phenomenon is called recalescence). The grain nucleation is also random with respect to the orientation of the grain. Thus, to distinguish between different grains, a characteristic misorientation angle is attributed to each grain with respect to one of the principal direction (Figure 22).

Dendritic grain growth is assumed to be primarily driven by thermal undercooling and curvature undercooling. The kinetic undercooling and solute undercooling are ignored for the present work, although they are known to be important especially when in case of liquids with high Peclet number. The adopted grain growth model is similar to that described by Gandin and Rappaz.[240]

The model focuses on the envelope outlining the dendrite tip positions. In grains with four dendritic arms as in (corresponding to $<11>$ direction), the envelope can be approximated as a square. The nucleation site for the grain shown in Figure 22 is labelled as ν, and the grain has already been growing for time t as shown by the (inner) square envelope. The current length of the dendrite tips at time t is shown by $L_{\nu,i}^{t}$ where $i = 1, 2, 3, 4$ are the four directions of growth. For the purpose of grain growth, the temperature inside the square envelope is assumed to be locally uniform. Typically, nucleation is spherical and a small incubation time is associated with each nucleus necessary to
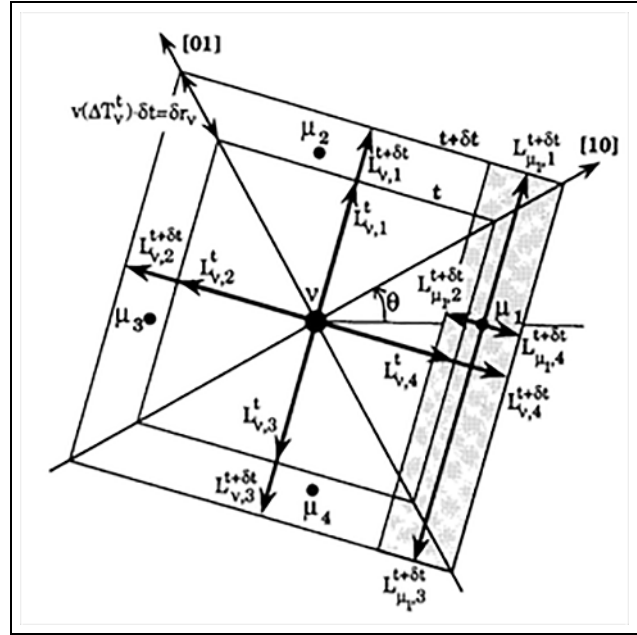
Figure 22. Schematic diagram illustrating the growth algorithm used in the cellular automata model for a dendritic grain whose $<10>$ direction is misoriented by an angle θ with respect to the horizontal axis of cellular automata network.[240]

generate the instability leading to dendritic growth. The incubation time is neglected here and the grains are assumed to be dendritic from start.

The growth of the grain is associated with the length of the dendrite tip which in turn depends upon the growth kinetics. For a grain nucleated at time t_n and experiencing an undercooling of ΔT, the length of dendrite tip is given by

$$
L_{\nu}^{t} = \int\limits_{t_n}^{t} \vartheta\left(\Delta T_{\nu}^{t'}\right)dt'
\tag{41}
$$

where ϑ is the velocity of the dendrite tip (i.e. interface velocity). The total undercooling ΔT is decomposed into a sum of two different terms

$$
\Delta T = \Delta T_t + \Delta T_r
\tag{42}
$$

with the contribution of thermal undercooling ΔT_t and curvature undercooling ΔT_r being expressed as

$$
\Delta T_t = \frac{\Delta H_f}{C_r}I_{\nu}(P_t)
\tag{43}
$$

$$
\Delta T_r = \frac{2\Gamma}{R}
\tag{44}
$$

where ΔH_f is the latent heat of fusion, C_r is the specific heat, P_t is thermal Peclet number, Γ is the Gibbs–Thomson coefficient defined as the ratio of the solid–liquid interfacial energy to the entropy of fusion, R is

the radius of the dendrite tip and I_v is the Ivantsov function expressed as

$$I_v(x) = xe^x \int_x^{\inf} \frac{e^{-z}}{z} dz \qquad (45)$$

The radius of curvature of the dendrite tip is a function of the thermal Peclet number and is given by

$$R = 4\pi^2 \Gamma \left[\frac{\Delta H_f}{C_r} P_t \xi_t \right]^{-1} \qquad (46)$$

$$\xi_t = 1 - \frac{1}{\sqrt{1 + \left(\frac{2\pi}{P_t}\right)^2}} \qquad (47)$$

$$P_t = \frac{\vartheta R}{2\alpha} \qquad (48)$$

where α is the thermal diffusivity. The velocity of the dendrite tip and the radius of dendrite tip, in this case, are expressed as functions of the undercooling.

The modelling of microstructure for SLM is performed using a sequentially coupled 3D FVADI thermal model[228] and a 2D Cellular Automata microstructure model. The cellular automata model and implementation of grain nucleation and grain growth models are explained below.

A cellular automata is a discrete model consisting of a regular grid of cells, each in one of a finite number of states. For each cell, a set of cells called its neighbourhood is defined relative to the specified cell. The two most common descriptions of neighbourhood are Moore's neighbourhood (all eight cells surrounding a square cell) and the von Neumann neighbourhood (the top, bottom, left and right adjacent cells). An initial state is selected by assigning a state for each cell. A new generation is then created according to some fixed rule that determines the new state of each cell in terms of the current state of the cell and the states of the cells in its neighbourhood. Typically, the rule for updating the state of cells is the same for each cell and does not change over time.

The grain nucleation phenomenon is modelled in the cellular automata model in a probabilistic manner. Each cell of the cellular automata model is prescribed a random probability of nucleation which indirectly corresponds to a random distribution of critical undercooling. For nucleation to take place in a cell ν

$$\delta n(\Delta T)_\nu * VCA_\nu \geq Prob(\nu) \qquad (49)$$

where VCA is the volume of the cellular automata and $Prob(\nu)$ is the randomly generated probability at cell ν.

In the current implementation, the mathematical function (rule) governing the cellular automata is based on the growth of grain, more specifically the growth of the dendritic arms of the crystal. The rules can be set as follows:

Rule 1: The dendritic arm of a cell can start to grow only if the cell has been nucleated or captured by an adjacent grain.
Rule 2: The dendritic arm of a cell in a direction can grow only if the adjacent cell in that direction is below the liquidus temperature and has not already been nucleated or captured by another grain.
Rule 3: Once captured by a dendritic arm from an adjacent cell, a cell gets the same state (misorientation) as the cell capturing it and is assumed to possess dendritic arms of same length as the capturing cell in the orthogonal direction to that of the capturing dendritic arm.

For the purpose of capturing an adjacent cell, the grain envelope must reach the centre of the adjacent cell. For the grain shown in Figure 22, this corresponds to the situation when

$$L_\nu^t = l(\cos\theta + |\sin\theta|) \qquad (50)$$

where θ is the misorientation angle of the capturing cell and l is the distance between the cells. Once captured, the length of the dendrite arm in captured cell is reset to match the dendrite lengths in orthogonal direction of the capturing cell. For example, if an adjacent cell μ is captured by the top dendrite arm of cell ν, the dendrite arm lengths in μ are given by

$$L_{\mu,\text{right}}^t = L_{\nu,\text{right}}^t \qquad (51)$$

$$L_{\mu,\text{left}}^t = L_{\nu,\text{left}}^t \qquad (52)$$

$$L_{\mu,\text{top}}^t = L_{\nu,\text{bottom}}^t = 0 \qquad (53)$$

As per the cellular automata rules, the growth of cell ν in the top direction would then stop and the grain growth in cell μ will develop based on the local undercooling in that cell. Thus, the non-isothermal conditions of grain growth are captured while ensuring the propagation of grain misorientation.

In the particular implementation, only equiaxed grains are considered, and therefore, the growth of dendrite arms in the four directions for a cell is the same and only based on the local undercooling. In case of columnar grains, however, the growth might be preferred along certain direction over the others.

The 3D FVADI and 2D CA models are coupled sequentially with the 3D FVADI model providing the temperature field. To take into account the release of latent heat, equivalent specific heat capacity values are used during calculations. The temperature field calculated from the 3D FVADI model thereby governs the

Table 1. Parameters for thermal model of single melt track formation.[237]

Parameters	Value
Power	120 W
FWHM	100×10^{-6} m
Powder bed porosity	0.35
Powder diameter	30×10^{-6} m
Scan speed	0.8 m/s
Chamber temperature	$200\,^{\circ}$C

Table 2. Parameters for microstructural model of single melt track formation.[237]

Parameters	Value
Maximum nucleation density (n_{max})	10^{16} m^{-3}
Mean undercooling (ΔT_μ)	25 K
Standard nucleation density distribution (ΔT_σ)	5 K
Number of grain misorientation states	48
Unit thermal undercooling ($\Delta H_f / C_p$)	523 K

undercooling occurring at each cell in the 2D CA model. As the thermal calculations are performed at a larger spatial and temporal discretization, the values are interpolated in the corresponding domains to match the requirements of the cellular automata. As a thumb rule, the spatial discretization of the CA model is near the order of the radius of dendritic tip, and the

time resolution is such that the dendrite tip can only grow till the next adjacent cell at a maximum chosen undercooling.

The centre-line microstructure of a single melt track is modelled using the 3D FVADI–2D CA model. The parameters used for the thermal model are shown in Table 1 and the parameters for the microstructural model in Table 2.

The thermal model was used on a domain of $1\,\text{mm} \times 1\,\text{mm} \times 1.5\,\text{mm}$ with elements of $10\,\mu\text{m}$ edge length in each direction. As the scan speed of the laser was high, the thermal model was solved at a time interval of 7.8125×10^{-7} ms which corresponds to 1/16th of the time taken by centre of laser beam to move from one element to the adjacent one. The 2D cellular automata model had square cells with edge length of $1.25\,\mu\text{m}$, thereby dividing each element from thermal model into eight cells in the microstructural model. The time steps for the microstructural was selected as 2.232×10^{-7} s based on the requirements for grain growth as discussed before.

Figure 23 shows the temperature field obtained from the thermal model at four time instances during the simulation of single melt track formation. The black rectangular borders shown on the figures correspond to the area selected for microstructure modelling using cellular automata. Figure 24 shows the solidification microstructure at the corresponding times. The grains are initially nucleated at the solid–liquid interface as can be seen in Figure 24. Although simulated on a
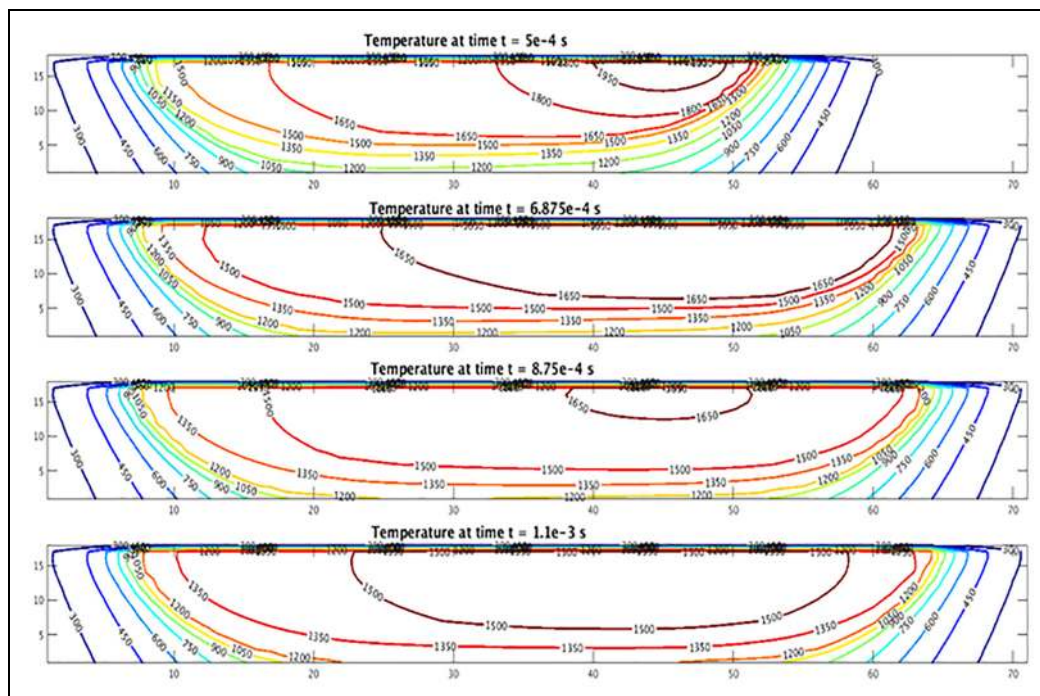
Figure 23. Centre-line temperatures at four time points during single track formation with SLM.[237]
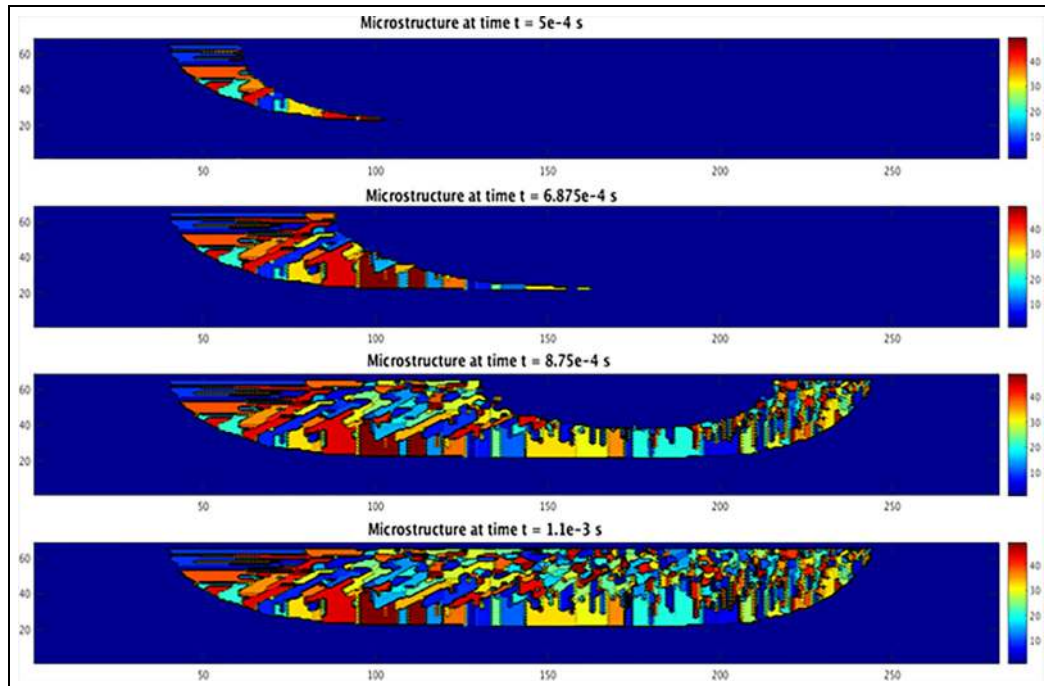
Figure 24. Evolution of centre-line microstructure at four time points during single track formation with SLM.[237]

structured grid, the grains maintained their misorientation during growth which resembles real grain growth mechanism. Most of the grains are seen to be oriented at a large angle to the direction of laser movement (also commonly observed phenomena), which is a result of the grains growing normal to the solidification isotherm.

For simulation of microstructures which can be validated against experimentally generated single track, the model would require several parameters which need to be determined experimentally such as the maximum nucleation density, the mean undercooling, the radius of unit thermal undercooling. In addition, the model would need to be extended to include solute diffusion and kinetic undercooling.

For comparison with single track which is allowed to cool under processing conditions, the model would also require to include the recrystallization occurring at β transus temperature from β to a martensitic α' phase followed by the decomposition into Widmanstatten plate-like or basketweave acicular α phase. As such modelling of solid-state phase transformation is an extensive research field in itself – wherein the challenge of predicting process-driven microstructure is tackled at different length and time scales. Along with cellular automata–based techniques, methodologies such as molecular dynamics, phase-field modelling, Monte Carlo Potts modelling and crystal plasticity have been used by researchers to predict microstructures across micro- to meso- to macro-length and time scales.

Figure 25 shows prediction of a single-phase equilibrium microstructure (from β to α' phase) through Monte Carlo simulations of two-dimensional Potts model.

The thermo-metallurgical model was able to predict the representative microstructure observed during single melt track formation on a loose powder bed using SLM. The small size of melt pool and the high cooling gradient, especially in case of low Peclet number materials, allows neglecting certain otherwise important terms from the grain growth models. However, it would be necessary to include them in case of high Peclet number material such as 316L steel. In addition, the evolution of solidification microstructure from SLM into the final $\alpha + \beta$ state will be the subsequent direction of work.

Conclusion

Modelling and simulation of manufacturing processes is a truly interdisciplinary field spanning mathematics, computer science, heat transfer, fluid and solid mechanics as well as materials science and manufacturing engineering. Models allow us to create mathematical representations of the system under investigation and simulate its properties and behaviour over time and under different conditions. This is an extremely powerful approach in planning and understanding experiments and producing predictions in designing manufacturing systems and increasing their efficiency. Modelling and simulation techniques are used in all
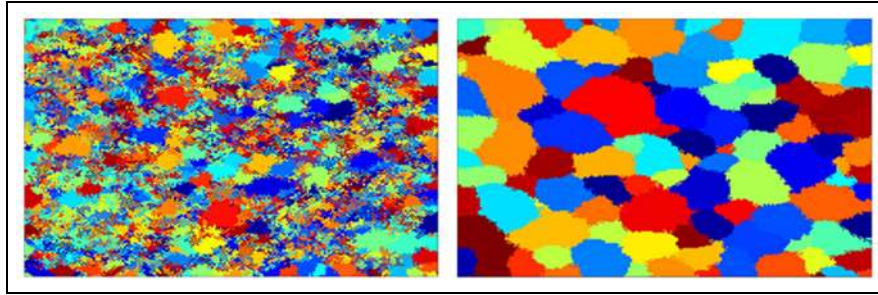
Figure 25. Monte Carlo simulation based on 2D Potts model for β to α' phase transformation: intermediate recrystallized microstructure (left) and predicted equilibrium microstructure (right).

realms of science and engineering and find endless industrial applications.

The present paper presents five cases of modelling different aspects of modern manufacturing processes ranging from fluid flow analysis (tape casting of ceramics and extrusion of polymers) over thermomechanical analysis (NIL of features on the surface of injection moulding dies and composite manufacturing) to thermo-metallurgical analysis in SLM. For some of these areas, selected results from numerical modelling have been compared with corresponding experimental findings and good agreement has been found. It is evident that models and simulations like the ones presented here will further increase their use in the future as an important part of analysing the effect of selected materials and process parameters on the subsequent performance of manufactured parts.

Declaration of conflicting interests

The author(s) declared no potential conflicts of interest with respect to the research, authorship and/or publication of this article.

Funding

The author(s) received no financial support for the research, authorship and/or publication of this article.

References

1. Hattel JH. Integrated modelling in materials and process technology. *Mater Sci Technol* 2008; 24: 137–148.
2. Shivpuri R. Advances in numerical modeling of manufacturing process: application to steel, aerospace and automotive industries. *T Indian I Metals* 2004; 57: 345–366.
3. Chan KS, Pericleous K and Cross M. Numerical simulation of flows encountered during mold-filling. *Appl Math Model* 1991; 15: 624–631.
4. Mirbagheri SH, Esmaeileian H, Serajzadeh S, et al. Simulation of melt flow in coated mould cavity in the casting process. *J Mater Process Technol* 2003; 142: 493–507.
5. Mirbagheri SMH, Dadashzadeh M, Serajzadeh S, et al. Modeling the effect of mould wall roughness on the melt flow simulation in casting process. *Appl Math Model* 2004; 28: 933–956.
6. Tavakoli R, Babaei R, Varahram N, et al. Numerical simulation of liquid/gas phase flow during mold filling. *Comput Methods Appl Mech Eng* 2006; 196: 697–713.
7. Reilly C, Green NR and Jolly MR. The present state of modeling entrainment defects in the shape casting process. *Appl Math Model* 2013; 37: 611–628.
8. Reilly C, Green NR, Jolly MR, et al. The modelling of oxide film entrainment in casting systems using computational modelling. *Appl Math Model* 2013; 37: 8451–8466.
9. MAGMA. http://www.magmasoft.com, 2017.
10. FLOW-3D. http://www.flow3d.com, 2017.
11. Zhang Z and Wu C. Effect of fluid flow in the weld pool on the numerical simulation accuracy of the thermal field in hybrid welding. *J Manufact Process* 2015; 20: 215–223.
12. Schmidt H, Hattel J and Wert J. An analytical model for the heat generation in friction stir welding. *Model Sim Mater Sci Eng* 2004; 12: 143.
13. Schmidt HB and Hattel JH. Thermal modelling of friction stir welding. *Scr Mater* 2008; 58: 332–337.
14. Schmidt HB and Hattel JH. A local model for the thermomechanical conditions in friction stir welding. *Model Sim Mater Sci Eng* 2005; 13: 77.
15. Sonne MR, Tutum CC, Hattel JH, et al. The effect of hardening laws and thermal softening on modeling residual stresses in FSW of aluminum alloy 2024-T3. *J Mater Process Technol* 2013; 213: 477–486.
16. Mishra S and DebRoy T. A heat-transfer and fluid-flow-based model to obtain a specific weld geometry using various combinations of welding variables. *J Appl Phys* 2005; 98: 044902.
17. He X, Gu F and Ball A. A review of numerical analysis of friction stir welding. *Prog Mater Sci* 2014; 65: 1–66.
18. Hattel JH, Sonne MR and Tutum CC. Modelling residual stresses in friction stir welding of Al alloys – a review of possibilities and future trends. *Int J Adv Manufact Technol* 2015; 76: 1793–1805.
19. Gafur MA, Haque MN and Prabhu KN. Effect of chill thickness and superheat on casting/chill interfacial heat transfer during solidification of commercially pure aluminium. *J Mater Process Technol* 2003; 133: 257–265.

20. Behnam MMJ, Davami P and Varahram N. Effect of cooling rate on microstructure and mechanical properties of gray cast iron. *Mater Sci Eng A* 2010; 528: 583–588.

21. Vijayaram TR, Sulaiman S, Hamouda AMS, et al. Numerical simulation of casting solidification in permanent metallic molds. *J Mater Process Technol* 2006; 178: 29–33.

22. Jabbari M and Hosseinzadeh A. Numerical modeling of coupled heat transfer and phase transformation for solidification of the gray cast iron. *Comput Mater Sci* 2013; 68: 160–165.

23. Howatt G, Breckenridge R and Brownlow J. Fabrication of thin ceramic sheets for capacitors. *J Am Ceram Soc* 1947; 30: 237–242.

24. Mistler RE and Twiname ER. *Tape casting: theory and practice*. Westerville, OH: American Ceramic Society, 2000.

25. Ring TA. A model of tape casting Bingham plastic and Newtonian fluids. *Adv Ceramics* 1989; 26: 569–576.

26. Loest H, Lipp R and Mitsoulis E. Numerical flow simulation of viscoplastic slurries and design criteria for a tape casting unit. *J Am Ceram Soc* 1994; 77: 254–262.

27. Pitchumani R and Karbhari VM. Generalized fluid flow model for ceramic tape casting. *J Am Ceram Soc* 1995; 78: 2497–2503.

28. Huang XY, Liu CY and Gong HQ. A viscoplastic flow modeling of ceramic tape casting. *Mater Manufact Process* 1997; 12: 935–943.

29. Terrones G, Smith PA, Armstrong TR, et al. Application of the Carreau model to tape-casting fluid mechanics. *J Am Ceram Soc* 1997; 80: 3151–3156.

30. Tok AIY, Boey FYC and Lam YC. Non-Newtonian fluid flow model for ceramic tape casting. *Mater Sci Eng A* 2000; 280: 282–288.

31. Joshi SC, Lam YC, Boey FYC, et al. Power law fluids and Bingham plastics flow models for ceramic tape casting. *J Mater Process Technol* 2002; 120: 215–225.

32. Zhang G, Wang Y and Ma J. Bingham plastic fluid flow model for ceramic tape casting. *Mater Sci Eng A* 2002; 337: 274–280.

33. Chou YT, Ko YT and Yan MF. Fluid flow model for ceramic tap casting. *J Am Ceram Soc* 1987; 70: 280–282.

34. Kim HJ, Krane MJM, Trumble KP, et al. Analytical fluid flow models for tape casting. *J Am Ceram Soc* 2006; 89: 2769–2775.

35. Jabbari M, Bulatova R, Hattel JH, et al. Quasi-steady state power law model for the flow of (LaSr)MnO ceramic slurry in tape casting. *J Mater Sci Technol* 2013; 29: 1080–1088.

36. Jabbari M and Hattel JH. Bingham plastic fluid flow model in tape casting of ceramics using two doctor blades – analytical approach. *Mater Sci Technol* 2014; 30: 283–288.

37. Loest H, Mitsoulis E and Spauszud S. Free surface measurements and numerical simulations of ceramic tape casting. *Interceram* 1993; 42: 80–84.

38. Gaskell PH, Rand B, Summers JL, et al. The effect of reservoir geometry on the flow within ceramic tape casters. *J Eur Ceram Soc* 1997; 17: 1185–1192.

39. Wonisch A, Polfer P, Kraft T, et al. A comprehensive simulation scheme for tape casting: from flow behavior to anisotropy development. *J Am Ceram Soc* 2011; 94: 2053–2060.

40. Jabbari M and Hattel JH. Numerical modeling of the side flow in tape casting of a non-Newtonian fluid. *J Am Ceram Soc* 2013; 96: 1414–1420.

41. Jabbari M, Bulatova R, Hattel JH, et al. An evaluation of interface capturing methods in a VOF based model for multiphase flow of a non-Newtonian ceramic in tape casting. *Appl Math Model* 2014; 38: 3222–3232.

42. Jabbari M, Spangenberg J and Hattel JH. Particle migration using local variation of the viscosity (LVOV) model in flow of a non-Newtonian fluid for ceramic tape casting. *Chem Eng Res Des* 2016; 109: 226–233.

43. Jabbari M, Bulatova R, Tok A, et al. Ceramic tape casting: a review of current methods and trends with emphasis on rheological behaviour and flow analysis. *Mater Sci Eng B* 2016; 212: 39–61.

44. Jacobsen S, Cepuritis R, Peng Y, et al. Visualizing and simulating flow conditions in concrete form filling using pigments. *Constr Build Mater* 2013; 49: 328–342.

45. Dinesen AR, Linderoth S, Pryds N, et al. *Magnetic regenerator, a method of making a magnetic regenerator, a method of making an active magnetic refrigerator and an active magnetic refrigerator*. US8061147 Patent, 2011.

46. Smith A, Bahl CRH, Bjørk R, et al. Materials challenges for high performance magnetocaloric refrigeration devices. *Adv Energy Mater* 2012; 2: 1288–1318.

47. Jabbari M, Spangenberg J and Hattel JH. Modeling of the interface behavior in functionally graded ceramics for magnetic refrigeration parts. *Int J Refrig* 2013; 36: 2403–2409.

48. Bulatova R, Jabbari MA, Kaiser MDN, et al. Thickness control and interface quality as functions of slurry formulation and casting speed in side-by-side tape casting. *J Eur Ceram Soc* 2014; 34: 4285–4295.

49. Martinez CJ and Lewis JA. Rheological, structural, and stress evolution of aqueous Al_2O_3: latex tape-cast layers. *J Am Ceram Soc* 2002; 85: 2409–2416.

50. Jabbari M and Hattel J. Modelling coupled heat and mass transfer during drying in tape casting with a simple ceramics–water system. *Drying Technol* 2016; 34: 244–253.

51. Mosthaf K, Baber K, Flemisch B, et al. A coupling concept for two-phase compositional porous-medium and single-phase compositional free flow. *Water Resour Res* 2011; 47: 1–19.

52. Baber K, Mosthaf K, Flemisch B, et al. Numerical scheme for coupling two-phase compositional porous-media flow and one-phase compositional free flow. *IMA J Appl Mathemat* 2012; 77: 887–909.

53. Mosthaf K, Helmig R and Or D. Modeling and analysis of evaporation processes from porous media on the REV scale. *Water Resour Res* 2014; 50: 1059–1079.

54. Jambhekar V, Schröder N, Helmig R, et al. Free–flow–porous-media coupling for evaporation-driven transport and precipitation of salt. *Trans Porous Media* 2015; 110: 251–280.

55. Jabbari M, Jambhekar V, Hattel J, et al. Drying of a tape-cast layer: numerical modelling of the evaporation process in a graded/layered material. *Int J Heat Mass Transfer* 2016; 103: 1144–1154.

56. Jabbari M, Nasirabadi P, Jambhekar V, et al. Drying of a tape-cast layer: numerical investigation of influencing parameters. *Int J Heat Mass Transfer* 2017; 108: 2229–2238.

57. Carneiro OS, Nóbrega JM, Pinho FT, et al. Computer aided rheological design of extrusion dies for profiles. *J Mater Process Technol* 2001; 114: 75–86.

58. Pittman JFT. Computer-aided design and optimization of profile extrusion dies for thermoplastics and rubber: a review. *Proc Inst Mech Eng E J Process Mech Eng* 2011; 225: 280–321.

59. Elgeti S, Probst M, Windeck C, et al. Numerical shape optimization as an approach to extrusion die design. *Finite Elem Anal Des* 2012; 61: 35–43.

60. Pauli L, Behr M and Elgeti S. Towards shape optimization of profile extrusion dies with respect to homogeneous die swell. *J Nonnewton Fluid Mech* 2013; 200: 79–87.

61. Gonçalves ND, Carneiro OS, Nóbrega JM, et al. Design of complex profile extrusion dies through numerical modeling. *J Nonnewton Fluid Mech* 2013; 200: 103–110.

62. Ettinger HJ, Pittman JFT and Sienz J. Optimization-driven design of dies for profile extrusion: parameterization, strategy, and performance. *Polym Eng Sci* 2013; 53: 189–203.

63. Siegbert R, Yesildag N, Frings M, et al. Individualized production in die-based manufacturing processes using numerical optimization. *Int J Adv Manufact Technol* 2014; 80: 851–858.

64. Denn MM. Extrusion instabilities and wall slip. *Ann Rev Fluid Mech* 2001; 33: 265–287.

65. Agassant JF, Arda DR, Combeaud C, et al. Polymer processing extrusion instabilities and methods for their elimination or minimisation. *Int Polym Process* 2006; 21: 239–255.

66. Achilleos E, Georgiou GC and Hatzikiriakos SG. On numerical simulation of polymer extrusion instabilities. *Appl Rheol* 2002; 12: 88–104.

67. Wang SQ, Drda PA and Inn YW. Exploring molecular origins of sharkskin, partial slip, and slope change in flow curves of linear low density polyethylene. *J Rheol* 1996; 40: 875–898.

68. Graham MD. The sharkskin instability of polymer melt flows. *Chaos* 1999; 9: 154–163.

69. Migler KB, Son Y, Qiao F, et al. Extensional deformation, cohesive failure, and boundary conditions during sharkskin melt fracture. *J Rheol* 2002; 46: 383–400.

70. Georgiou GC and Crochet MJ. Time-dependent compressible extrudate-swell problem with slip at the wall. *J Rheol* 1994; 38: 1745–1755.

71. Georgiou GC. On the stability of the shear flow of a viscoelastic fluid with slip along the fixed wall. *Rheol Acta* 1996; 35: 39–47.

72. Brasseur E, Fyrillas MM, Georgiou GC, et al. The time-dependent extrudate-swell problem of an Oldroyd-B fluid with slip along the wall. *J Rheol* 1998; 42: 549–566.

73. Taliadorou E, Georgiou GC and Alexandrou AN. A two-dimensional numerical study of the stick–slip extrusion instability. *J Nonnewton Fluid Mech* 2007; 146: 30–44.

74. Piau JM and Kissi NE. Measurement and modelling of friction in polymer melts during macroscopic slip at the wall. *J Nonnewton Fluid Mech* 1994; 54: 121–142.

75. Park HE, Lim ST, Smillo F, et al. Wall slip and spurt flow of polybutadiene. *J Rheol* 2008; 52: 1201–1239.

76. Leonov AI. On the dependence of friction force on sliding velocity in the theory of adhesive friction of elastomers. *Wear* 1990; 141: 137–145.

77. Yarin AL and Graham MD. A model for slip at polymer/solid interfaces. *J Rheol* 1998; 42: 1491–1504.

78. Dubbeldam JLA and Molenaar J. Self-consistent dynamics of wall slip. *Phys Rev E* 2003; 67: 011803.

79. Hatzikiriakos SG. Wall slip of molten polymers. *Prog Polym Sci* 2012; 37: 624–643.

80. Piau JM, Kissi N, Toussaint F, et al. Distortions of polymer melt extrudates and their elimination using slippery surfaces. *Rheol Acta* 1995; 34: 40–57.

81. Shore JD, Ronis D, Piché L, et al. Theory of melt fracture instabilities in the capillary flow of polymer melts. *Phys Rev E* 1997; 55: 2976–2792.

82. Aarts ACT and de Ven AAFV. The occurrence of periodic distortions in the extrusion of polymeric melts. *Continuum Mech Thermodyn* 1999; 11: 113–139.

83. Piau JM, Kissi NE and Tremblay B. Influence of upstream instabilities and wall slip on melt fracture and sharkskin phenomena during silicones extrusion through orifice dies. *J Nonnewton Fluid Mech* 1990; 34: 145–180.

84. Nigen S, Kissi NE, Piau JM, et al. Velocity field for polymer melts extrusion using particle image velocimetry: stable and unstable flow regimes. *J Nonnewton Fluid Mech* 2003; 112: 177–202.

85. Goutille Y and Guillet J. Influence of filters in the die entrance region on gross melt fracture: extrudate and flow visualization. *J Nonnewton Fluid Mech* 2002; 102: 19–36.

86. Meulenbroek B, Storm C, Bertola V, et al. Intrinsic route to melt fracture in polymer extrusion: a weakly nonlinear subcritical instability of viscoelastic Poiseuille flow. *Phys Rev Lett* 2003; 90: 024502.

87. Bertola V, Meulenbroek B, Wagner C, et al. Experimental evidence for an intrinsic route to polymer melt fracture phenomena: a nonlinear instability of viscoelastic Poiseuille flow. *Phys Rev Lett* 2003; 90: 114502.

88. Larson RG. Instabilities in viscoelastic flows. *Rheol Acta* 1992; 31: 213–263.

89. Shaqfeh ESG. Purely elastic instabilities in viscometric flows. *Ann Rev Fluid Mech* 1996; 28: 129–185.

90. Morozov AN and van Saarloos W. An introductory essay on subcritical instabilities and the transition to turbulence in visco-elastic parallel shear flows. *Phys Reports* 2007; 447: 112–143.

91. Crochet MJ and Keunings R. Finite element analysis of die swell of a highly elastic fluid. *J Nonnewton Fluid Mech* 1982; 10: 339–356.

92. Normandin M, Clermont JR, Guillet J, et al. Three-dimensional extrudate swell experimental and numerical study of a polyethylene melt obeying a memory-integral equation. *J Nonnewton Fluid Mech* 1999; 87: 1–25.

93. Karapetsas G and Tsamopoulos J. Steady extrusion of viscoelastic materials from an annular die. *J Nonnewton Fluid Mech* 2008; 154: 136–152.

94. Ganvir V, Lele A, Thaokar R, et al. Prediction of extrudate swell in polymer melt extrusion using an Arbitrary Lagrangian Eulerian (ALE) based finite element method. *J Nonnewton Fluid Mech* 2009; 156: 21–28.

95. Russo G and Phillips TN. Spectral element predictions of die-swell for Oldroyd-B fluids. *Comput Fluid* 2011; 43: 107–118.

96. Scardovelli R and Zaleski S. Direct numerical simulation of free-surface and interfacial flow. *Ann Rev Fluid Mech* 1999; 31: 567–603.

97. Tomé MF, Grossi L, Castelo A, et al. Die-swell, splashing drop and a numerical technique for solving the Oldroyd B model for axisymmetric free surface flows. *J Nonnewton Fluid Mech* 2007; 141: 148–166.

98. Tomé MF, Castelo A, Ferreira VG, et al. A finite difference technique for solving the Oldroyd-B model for 3D-unsteady free surface flows. *J Nonnewton Fluid Mech* 2008; 154: 179206.

99. Tomé MF, Castelo A, Afonso AM, et al. Application of the log-conformation tensor to three-dimensional time-dependent free surface flows. *J Nonnewton Fluid Mech* 2012; 175: 44–54.

100. Tanner RI. A theory of die-swell. *J Polym Sci A Polym Phys* 1970; 8: 2067–2078.

101. Tanner RI. A theory of die-swell revisited. *J Nonnewton Fluid Mech* 2005; 129: 85–87.

102. Vlachopoulos J, Horie M and Lidorikis S. An evaluation of expressions predicting die swell. *Trans Soc Rheol* 1972; 16: 669–685.

103. Keunings R. On the high Weissenberg number problem. *J Nonnewton Fluid Mech* 1986; 20: 209–226.

104. Walters K and Webster MF. The distinctive CFD challenges of computational rheology. *Int J Numer Methods Fluids* 2003; 43: 577–596.

105. Hulsen MA, van Heel APG and van den Brule BHAA. Simulation of viscoelastic flows using Brownian configuration fields. *J Nonnewton Fluid Mech* 1997; 70: 79–101.

106. Lee J, Yoon S, Kwon Y, et al. Practical comparison of differential viscoelastic constitutive equations in finite element analysis of planar 4:1 contraction flow. *Rheol Acta* 2004; 44: 188–197.

107. Fattal R and Kupferman R. Constitutive laws for the matrix-logarithm of the conformation tensor. *J Nonnewton Fluid Mech* 2004; 123: 281–285.

108. Fattal R and Kupferman R. Time-dependent simulation of viscoelastic flows at high Weissenberg number using the log-conformation representation. *J Nonnewton Fluid Mech* 2005; 126: 23–37.

109. Hulsen MA, Fattal R and Kupferman R. Flow of viscoelastic fluids past a cylinder at high weissenberg number: stabilized simulations using matrix logarithms. *J Nonnewton Fluid Mech* 2005; 127: 27–39.

110. Renardy M. Current issues in non-Newtonian flows: a mathematical perspective. *J Nonnewton Fluid Mech* 2000; 90: 243–259.

111. Kwon Y. Melt fracture modeled as 2D elastic flow instability. *Rheol Acta* 2015; 54: 445–453.

112. Leonov AI. Nonequilibrium thermodynamics and rheology of viscoelastic polymer media. *Rheol Acta* 1976; 15: 85–98.

113. Osher S and Fedkiw RP. Level set methods: an overview and some recent results. *J Comput Phys* 2001; 169: 463–502.

114. Comminal R. *Numerical simulation of viscoelastic free-surface flows using a streamfunction/log-conformation formulation and the volume-of-fluid method.* PhD Thesis, Technical University of Denmark, Kongens Lyngby, 2015.

115. Comminal R, Spangenberg J and Hattel JH. A two-phase flow solver for incompressible viscous fluids, using a pure streamfunction formulation and the volume of fluid technique. *Def Diff Forum* 2014; 348: 9–19.

116. Kupferman R. A central-difference scheme for a pure stream function formulation of incompressible viscous flow. *SIAM J Sci Comput* 2001; 23: 1–18.

117. Wang S and Zhang X. An immersed boundary method based on discrete stream function formulation for two- and three-dimensional incompressible flows. *J Comput Phys* 2011; 230: 3479–3499.

118. Comminal R, Spangenberg J and Hattel JH. Robust simulations of viscoelastic flows at high weissenberg numbers with the streamfunction/log-conformation formulation. *J Nonnewton Fluid Mech* 2015; 223: 37–61.

119. Baran I, Akkerman R and Hattel JH. Modelling the pultrusion process of an industrial L-shaped composite profile. *Compos Struct* 2014; 118: 37–48.

120. Comminal R, Spangenberg J and Hattel JH. Cellwise conservative unsplit advection for the volume of fluid method. *J Comput Phys* 2015; 283: 582–608.

121. Xie X and Pasquali M. A new, convenient way of imposing open-flow boundary conditions in two-and three-dimensional viscoelastic flows. *J Nonnewton Fluid Mech* 2004; 122: 159–176.

122. Kalika DS and Denn MM. Wall slip and extrudate distortion in linear low-density polyethylene. *J Rheol* 1987; 31: 815–834.

123. Pokroy B, Epstein AK, Persson-Gulda MCM, et al. Fabrication of bioinspired actuated nanostructures with arbitrary geometry and stiffness. *Adv Mater* 2009; 21: 463–469.

124. Barthlott W and Neinhuis C. Purity of the sacred lotus, or escape from contamination in biological surfaces. *Planta* 1997; 202: 1–8.

125. Ruibal R and Ernst V. The structure of the digital setae of lizards. *J Morphol* 1965; 117: 271–293.

126. Kolle M, Salgard-Cunha PM, Scherer MR, et al. Mimicking the colourful wing scale structure of the *Papilio blumei* butterfly. *Nat Nanotechnol* 2010; 5: 511–515.

127. Christiansen AB, Højlund-Nielsen E, Clausen J, et al. Imprinted and injection-molded nano-structured optical surfaces. *SPIE Nanosci + Eng* 2013; 8818: 881803.

128. Parker AR. 515 million years of structural colour. *J Opt A Pure Appl Op* 2000; 2: R15–R28.

129. Kinoshita S, Yoshioka S and Miyazaki J. Physics of structural colors. *Rep Prog Phys* 2008; 71: 076401.

130. Sonne MR, Smistrup K, Hannibal M, et al. Modeling and simulation of the deformation process of PTFE flexible stamps for nanoimprint lithography on curved surfaces. *J Mater Process Technol* 2015; 216: 418–429.

131. Fernández A, Medina J, Benkel C, et al. Residual layer-free Reverse Nanoimprint Lithography on silicon and metal-coated substrates. *Microelectron Eng* 2015; 141: 56–61.

132. Højlund-Nielsen E, Zhu X, Carstensen MS, et al. Polarization-dependent aluminum metasurface operating at 450 nm. *Opt Express* 2015; 23: 28829–28835.

133. Chou SY, Krauss PR and Renstrom PJ. Imprint of sub-25 nm vias and trenches in polymers. *Appl Phys Lett* 1995; 67: 3114–3116.

134. Sonne M, Cech J, Pranov H, et al. Modelling the deformations during the manufacturing of nanostructures on non-planar surfaces for injection moulding tool inserts. *J Micromech Microeng* 2016; 26: 035014.

135. Cech J, Pranov H, Kofod G, et al. Surface roughness reduction using spray-coated hydrogen silsesquioxane reflow. *Appl Surf Sci* 2013; 280: 424–430.

136. Sonne MR, Cech J, Pranov H, et al. Modelling the deformation of nickel foil during manufacturing of nanostructures on injection moulding tool inserts. *AIP Conf Proc* 2016; 1769: 090003.

137. Selimis A, Mironov V and Farsari M. Direct laser writing: principles and materials for Scaffold 3D printing. *Microelectron Eng* 2015; 132: 83–89.

138. Plast4Future. http://www.plast4future.eu/, 2015.

139. Sonne MR, Hattel JH and Kristensen A. Addressing the mechanical deformation of flexible stamps for nanoimprint lithography on double-curved surfaces. In: *11Th international conference on nanoimprint and nanoprint technology (NNT 2012)*, Napa, CA, 24–26 October 2012.

140. Højlund-Nielsen E, Weirich J, Nørregaard J, et al. Angle-independent structural colors of silicon. *J Nanophotonics* 2014; 8: 083988.

141. Taylor H, Lam YC and Boning D. A computationally simple method for simulating the micro-embossing of thermoplastic layers. *J Micromech Microeng* 2009; 19: 075007.

142. Farshchian B, Amirsadeghi A, Hurst SM, et al. Deformation behavior in 3D molding: experimental and simulation studies. *J Micromech Microeng* 2012; 22: 115027.

143. Hirai Y, Konishi T, Yoshikawa T, et al. Simulation and experimental study of polymer deformation in nanoimprint lithography. *J Vac Sci Technol B* 2004; 22: 3288–3293.

144. Marín JMR, Rasmussen HK and Hassager O. 3D simulation of nano-imprint lithography. *Nanoscale Res Lett* 2010; 5: 274–278.

145. Schift H. Nanoimprint lithography: an old story in modern times? A review. *J Vac Sci Technol B* 2008; 26: 458–480.

146. Bergström J and Hilbert L. A constitutive model for predicting the large deformation thermomechanical behavior of fluoropolymers. *Mech Mater* 2005; 37: 899–913.

147. Rae P and Brown E. The properties of poly (tetrafluoroethylene)(PTFE) in tension. *Polymer* 2005; 46: 8128–8140.

148. Rae P and Dattelbaum D. The properties of poly (tetrafluoroethylene)(PTFE) in compression. *Polymer* 2004; 45: 7615–7625.

149. Buckley DH and Johnson RL. Friction and wear of nickel-aluminum alloys and some sulfur-modified steels in vacuum to 10^{-9} millimeter of mercury. Technical Report (DTIC Document), DTIC, Fort Belvoir, VA, 1964.

150. Myshkin N, Petrokovets M and Kovalev A. Tribology of polymers: adhesion, friction, wear, and mass-transfer. *Tribol Int* 2006; 38: 910–921.

151. Samyn P and Schoukens G. Experimental extrapolation model for friction and wear of polymers on different testing scales. *Int J Mech Sci* 2008; 50: 1390–1403.

152. Esfahani MN, Sonne MR, Hattel JH, et al. Thermo-coupled surface Cauchy–Born theory: an engineering finite element approach to modeling of nanowire thermomechanical response. *Mech Mater* 2016; 94: 46–52.

153. Mendels DA. Multi-scale modelling of nano-imprint lithography. In: *SPIE (International Society for Optics and Photonics) 31st international symposium on advanced lithography*, San Jose, CA, 19–24 February 2006, p. 615113. Washington, DC: SPIE.

154. Schapery RA. On the characterization of nonlinear viscoelastic materials. *Polym Eng Sci* 1969; 9: 295–310.

155. Khan A and Zhang H. Finite deformation of a polymer: experiments and modeling. *Int J Plasticity* 2001; 17: 1167–1188.

156. Kletschkowski T, Schomburg U and Bertram A. Computational analysis of PTFE shaft seals. *Comput Mater Sci* 2005; 32: 392–399.

157. Johnson GR and Cook WH. A constitutive model and data for metals subjected to large strains, high strain rates and high temperatures. In: *Proceedings of the Seventh International Symposium on Ballistics*, Vol. 21, The Hague, The Netherlands, 19–21 April 1983, pp.541–547.

158. Sonne MR and Hattel JH. Modeling the constitutive and frictional behavior of PTFE flexible stamps for nanoimprint lithography. *Microelectron Eng* 2013; 106: 1–8.

159. Brøndsted P, Lilholt H and Lystrup A. Composite materials for wind power turbine blades. *Ann Rev Mater Res* 2005; 35: 505–538.

160. Baran I. *Pultrusion: state-of-the-art process models.* Shrewsbury: Smithers Rapra, 2015.

161. Baran I. Pultrusion processes for composite manufacture. In: Boisse P (ed.) *Advances in composites manufacturing and process design.* Cambridge: Woodhead Publishing, 2015, pp.379–314.

162. Korotkov V, Chekanov Y and Rozenberg B. The simultaneous process of filament winding and curing for polymer composites. *Compos Sci Tech* 1993; 47: 383–388.

163. Zhao L, Mantell S, Cohen D, et al. Finite element modeling of the filament winding process. *Compos Struct* 2001; 52: 499–510.

164. Ruiz E and Trochu F. Numerical analysis of cure temperature and internal stresses in thin and thick RTM parts. *Composites Part A* 2005; 36: 806–826.

165. Khoun L and Hubert P. Investigation of the dimensional stability of carbon epoxy cylinders manufactured by resin transfer moulding. *Composites Part A* 2010; 41: 116–124.

166. Svanberg J, Altkvist C and Nyman T. Prediction of shape distortions for a curved composite C-spar. *J Reinforced Plast Compos* 2005; 24: 323–339.

167. Jabbari M, Jambhekar V, Gersborg A, et al. Numerical modelling of the flow in the resin infusion process on the REV scale: a feasibility study. *AIP Conf Proc* 2016; 1738: 030051.

168. Nielsen MW. *Predictions of process induced shape distortions and residual stresses in large fibre reinforced composite laminates.* PhD Thesis, Technical University of Denmark, Kongens Lyngby, 2012.

169. Mallick PK. *Fiber-reinforced composites: materials, manufacturing, and design.* New York: CRC Press, 2007.

170. Wisnom M, Gigliotti M, Ersoy N, et al. Mechanisms generating residual stresses and distortion during manufacture of polymer-matrix composite structures. *Compos Part A Appl Sci Manufact* 2006; 37: 522–529.

171. Nielsen MW, Schmidt JW, Hattel JH, et al. In situ measurement using FBGs of process-induced strains during curing of thick glass/epoxy laminate plate: experimental results and numerical modelling. *Wind Energy* 2013; 16: 1241–1257.

172. Tutum CC, Baran I and Hattel JH. Utilizing multiple objectives for the optimization of the pultrusion process. *Key Eng Mater* 2013; 554–557: 2165–2174.

173. Baran I, Tutum CC and Hattel JH. The internal stress evaluation of the pultruded blades for a Darrieus wind turbine. *Key Eng Mater* 2013; 554–557: 2127–2137.

174. Johnston AA. *An integrated model of the development of process-induced deformation in autoclave processing of composite structures.* PhD Thesis, The University of British Columbia, Vancouver, BC, Canada, 1997.

175. Nielsen MW, Hattel JH, Andersen TL, et al. Experimental determination and numerical modeling of process induced strains and residual stresses in thick glass/epoxy laminate. In: *ECCM15: 15th European conference on composite materials*, Venice, 24–28 June 2012.

176. Nielsen MW, Schmidt JW, Høgh JH, et al. Life cycle strain monitoring in glass fibre reinforced polymer laminates using embedded fibre Bragg grating sensors from manufacturing to failure. *J Compos Mater* 2014; 48: 365–381.

177. Baran I, Akkerman R and Hattel JH. Material characterization of a polyester resin system for the pultrusion process. *Compos Part B Eng* 2014; 64: 194–201.

178. Bogetti T and Gillespie J. Process-induced stress and deformation in thick-section thermoset composite laminates. *J Compos Mater* 1992; 26: 626–660.

179. Baran I, Cinar K, Ersoy N, et al. A review on the mechanical modeling of composite manufacturing processes. *Arch Comput Methods E* 2016; 24: 365–395.

180. Whitney JM and McCullough RL. Micromechanical material modeling. In: Leif A. Carlsson (ed.) *Delaware composites design encyclopaedia*. Lancaster: Technomic Publishing Co, 1990.

181. Hackett R and Prasad S. Pultrusion process modelling. In: Newaz GM (ed.) *Advances in thermoplastic matrix composite materials (ASTM STP 1044)*. West Conshohocken, PA: ASTM, 1989, pp.62–70.

182. Batch G and Macosko C. A computer analysis of temperature and pressure distributions in a pultrusion die. In: *Proceedings of 42nd annual conference, composites institute,* Society of Plastics Industry Inc, Washington, DC, 2–6 February 1987. Technomic Publishing Company.

183. Sarrionandia M, Mondragn I, Moschiar S, et al. Heat transfer for pultrusion of a modified acrylic/glass reinforced composite. *Polymer Compos* 2002; 23: 21–27.

184. Ahmed F, Joshi S and Lam Y. Three-dimensional FE-NCV modeling of thermoplastic composites pultrusion. *J Thermoplast Compos* 2004; 17: 447–462.

185. Carlone P, Palazzo G and Pasquino R. Pultrusion manufacturing process development by computational modelling and methods. *Mathemat Comp Model* 2006; 44: 701–709.

186. Chachad Y, Roux J and Vaughan J. Manufacturing model for three dimensional pultruded graphite epoxy composites. *Compos Part A Appl Sci Manufact* 1996; 27: 201–210.

187. Ding Z, Li S and Lee L. Influence of heat transfer and curing on the quality of pultruded composites II: modeling and simulation. *Polymer Compos* 2002; 23: 957–969.

188. Suratno B, Ye L and Mai Y. Simulation of temperature and curing profiles in pultruded composite rods. *Compos Sci Tech* 1998; 58: 191–197.

189. Baran I, Hattel JH and Akkerman R. Investigation of process induced warpage for pultrusion of a rectangular hollow profile. *Compos Part B Eng* 2015; 68: 365–374.

190. Baran I, Hattel JH and Akkerman R. Investigation of the spring-in of a pultruded L-shaped profile for various processing conditions and thicknesses. *Key Eng Mater* 2014; 611–612: 273–279.

191. Baran I, Hattel JH, Akkerman R, et al. Mechanical modelling of pultrusion process: 2D and 3D numerical approaches. *Appl Compos Mater* 2015; 22: 99–118.

192. Carlone P, Baran I, Hattel JH, et al. Computational approaches for modeling the multiphysics in pultrusion process. *Adv Mech Eng* 2013; 5: 301875.

193. Baran I. Analysis of pultrusion process for thick glass/polyester composites: transverse shear stress formations. *Adv Manuf Polymer Comp Sci* 2016; 2: 124–132.

194. Liu X and Mahadevan S. Ultimate strength failure probability estimation of composite structures. *J Reinforced Plast Compos* 2000; 19: 403–426.

195. Baran I, Tutum CC and Hattel JH. Reliability estimation of the pultrusion process using the first-order reliability method (form). *Appl Compos Mater* 2013; 20: 639–653.

196. Baran I, Tutum CC and Hattel JH. Probabilistic analysis of a thermosetting pultrusion process. *Sci Eng Compos Mater* 2014; 23: 67–76.

197. Li J, Joshi S and Lam Y. Curing optimization for pultruded composite sections. *Compos Sci Tech* 2002; 62: 457–467.

198. Joshi S, Lam Y and Tun U. Improved cure optimization in pultrusion with pre-heating and die-cooler temperature. *Compos Part A Appl Sci Manufact* 2003; 34: 1151–1159.

199. Tutum CC, Baran I and Deb K. Optimum design of pultrusion process via evolutionary multi-objective optimization. *Int J Adv Manufact Technol* 2014; 72: 1205–1217.

200. Tutum CC, Deb K and Baran I. Constrained efficient global optimization for pultrusion process. *Mater Manufact Process* 2015; 30: 538–551.

201. Mioković T, Schulze V, Vöhringer O, et al. Prediction of phase transformations during laser surface hardening of AISI 4140 including the effects of inhomogeneous austenite formation. *Mater Sci Eng A* 2006; 435: 547–555.

202. Pietrzyk M. Through-process modelling of microstructure evolution in hot forming of steels. *J Mater Process Technol* 2002; 125: 53–62.

203. Yang H, Wu C, Li H, et al. Review on cellular automata simulations of microstructure evolution during metal forming process: grain coarsening, recrystallization and phase transformation. *Sci China Technol Sci* 2011; 54: 2107–2118.

204. Zhao HZ, Liu XH and Wang GD. Progress in modeling of phase transformation kinetics. *J Iron Steel Res Int* 2006; 13: 68–73.

205. Xiao N, Chen Y, Li D, et al. Progress in mesoscopic modeling of microstructure evolution in steels. *Sci China Technol Sci* 2012; 55: 341–356.

206. Schulze V, Uhlmann E, Mahnken R, et al. Evaluation of different approaches for modeling phase transformations in machining simulation. *Prod Eng* 2015; 9: 437–449.

207. Klocke F, Mohammadnejad M, Zeis M, et al. Potentials of the phase field approach for modeling modifications in material microstructure during electrical discharge machining. *Procedia CIRP* 2016; 42: 703–708.

208. Steinbach I. Phase-field model for microstructure evolution at the mesoscopic scale. *Ann Rev Mater Res* 2013; 43: 89–107.

209. Simonelli M, Tse YY and Tuck C. Microstructure of Ti-6Al-4V produced by selective laser melting. *J Phys* 2012; 371: 012084.

210. Simonelli M, Tse YY and Tuck C. Microstructure and mechanical properties of Ti-6A1-4V fabricated by selective laser melting. *Suppl Proceed Mater Process Inter* 2012; 1: 863–870.

211. Huaixue L, Baiying H, Fan S, et al. Microstructure and tensile properties of Ti-6Al-4V alloys fabricated by selective laser melting. *Rare Metal Mater Eng* 2013; 42: 209–212.

212. Simonelli M, Tse YY and Tuck C. On the texture formation of selective laser melted Ti-6Al-4V. *Metall Mater Trans A* 2014; 45: 2863–2872.

213. Fan Z, Sparks TE, Liou F, et al. Numerical simulation of the evolution of solidification microstructure in laser deposition. In: *Proceedings of the 18th annual solid freeform fabrication symposium*, Austin, TX, 6–8 August, 2007.

214. Zhang J, Liou F, Seufzer W, et al. Probabilistic simulation of solidification microstructure evolution during laser-based metal deposition 2013. In: *SFF Conference Proceedings Annual International Solid Freeform Fabrication Symposium*, Austin, TX, 12–14 August 2013.

215. Over C, Meiners W, Wissenbach K, et al. Selective laser melting: a new approach for the direct manufacturing of metal parts and tools. In: *Proceedings of the international conferences on LANE*, Nuremberg, 28–31 August 2001, pp.391–398. Meisenbach GmbH.

216. Frazier WE. Metal additive manufacturing: a review. *J Mater Eng Perform* 2014; 23: 1917–1928.

217. Uriondo A, Esperon-Miguez M and Perinpanayagam S. The present and future of additive manufacturing in the aerospace sector: a review of important aspects. *Proc Inst Mech Eng G J Aerosp Eng* 2015; 229: 2132–2147.

218. Bourell DL, Leu MC and Rosen DW. *Roadmap for additive manufacturing: identifying the future of freeform processing*. Austin, TX: The University of Texas at Austin, 2009, pp.11–15.

219. Coopers PW. *3D printing and the new shape of industrial manufacturing*. Arlington, VA: PWC, 2014.

220. Cruz MF and Borille AV. Decision methods application to compare conventional manufacturing process with metal additive manufacturing process in the aerospace industry. *J Braz Soc Mech Sci Eng* 2017; 39: 177–193.

221. Ford S and Despeisse M. Additive manufacturing and sustainability: an exploratory study of the advantages and challenges. *J Clean Prod* 2016; 137: 1573–1587.

222. Bourell DL. Perspectives on additive manufacturing. *Ann Rev Mater Res* 2016; 46: 1–18.

223. Mounsey S, Hon B and Sutcliffe C. Performance modelling and simulation of metal powder bed fusion production system. *CIRP Ann Manuf Techn* 2016; 65: 421–424.

224. Schoinochoritis B, Chantzis D and Salonitis K. Simulation of metallic powder bed additive manufacturing processes with the finite element method: a critical review. *Proc Inst Mech Eng, B J Eng Manuf* 2015; 231: 96–117.

225. Roberts IA, Wang C, Esterlein R, et al. A three-dimensional finite element analysis of the temperature field during laser melting of metal powders in additive layer manufacturing. *Int J Mach Tools Manu* 2009; 49: 916–923.

226. Mohanty S, Tutum CC and Hattel JH. Cellular scanning strategy for selective laser melting: evolution of optimal grid-based scanning path and parametric approach to thermal homogeneity. In: *SPIE LASE*, San Francisco, CA, 6–7 February 2013, p. 86080M. Washington, DC: International Society for Optics and Photonics.

227. Mohanty S and Hattel JH. Cellular scanning strategy for selective laser melting: capturing thermal trends with a low-fidelity, pseudo-analytical model. *Math Prob Eng* 2014; 2014: 715058.

228. Mohanty S and Hattel JH. Numerical model based reliability estimation of selective laser melting process. *Phys Proc* 2014; 56: 379–389.

229. Gusarov AV, Yadroitsev I, Bertrand P, et al. Heat transfer modelling and stability analysis of selective laser melting. *Appl Surf Sci* 2007; 254: 975–979.

230. Mohanty S and Hattel JH. A finite volume volume alternate direction implicit approach to modelling selective laser melting. In: *Proceedings of 32nd international congress on applications of lasers and electro-optics*, Miami, FL, 6–10 October 2014. Miami, FL: LIA.

231. Sih SS and Barlow JW. The prediction of the emissivity and thermal conductivity of powder beds. *Particul Sci Technol* 2004; 22: 427–440.

232. Sih SS and Barlow JW. Emissivity of powder beds. In: *Solid freeform fabrication symposium proceedings, Vol. 6*, Center for Materials Science and Engineering,

Departments of Mechanical Engineering and Chemical Engineering, The University of Texas at Austin, Austin, TX, 7–9 August 1995, pp.7–9.

233. Sih SS and Barlow JW. The prediction of the thermal conductivity of powders. In: Marcus H, Beaman J, Bourell D, et al. (eds) *Proceedings of the 6th annual SFF symposium*. Austin, TX: The University of Texas at Austin, 1995, pp.397–401.

234. Mohanty S and Hattel JH. Reducing residual stresses and deformations in selective laser melting through multilevel multiscale optimization of cellular scanning strategy. In: *SPIE LASE*, San Francisco, CA, 15–18 February 2016, p. 97380Z. Washington, DC: International Society for Optics and Photonics.

235. Mohanty S and Hattel J. Effect of uncertainty in processing parameters on the microstructure of single melt tracks formed by selective laser melting. In: *International congress proceedings on applications of lasers & electro-optics*, San Diego, CA, 19–23 October 2014. LIA.

236. Mohanty S and Hattel JH. Improving accuracy of overhanging structures for selective laser melting through reliability characterization of single track formation on thick powder beds. In: *SPIE LASE*, San Francisco, CA, 15–18 February 2016, p.97381B. Washington, DC: International Society for Optics and Photonics.

237. Mohanty S and Hattel JH. Laser additive manufacturing of multimaterial tool inserts: a simulation-based optimization study. *Proc of SPIE* 2017; 10095: 100950G-1.

238. Grong Ø and Shercliff HR. Microstructural modelling in metals processing. *Prog Mater Sci* 2002; 47: 163–282.

239. Oldfield W. A quantitative approach to casting solidification: freezing of cast iron. *Trans Am Soc Metal* 1966; 59: 945–960.

240. Gandin CA and Rappaz M. A coupled finite element-cellular automaton model for the prediction of dendritic grain structures in solidification processes. *Acta Metall Mater* 1994; 42: 2233–2246.